9-30-2007

GNEP Quarterly Input – UNLV July 1 through September 30, 2007

Harry Reid Center for Environmental Studies. Nuclear Science and Technology Division

GNEP Quarterly Input – UNLV
July 1 through September 30, 2007

1.0 University of Nevada, Las Vegas (UNLV)

UNLV Transmutation Research Program. The University of Nevada, Las Vegas supports the Global Nuclear Energy Partnership (GNEP) through research and development of technologies for economic and environmentally sound refinement of spent nuclear fuel. The UNLV program has four components: infrastructure, international collaboration, student-based research, and management and program support. Management and program support highlights are the following:

- Administrative and financial management of the UNLV Transmutation Research Program.
- UNLV hosted the GNEP Safeguards Working Group meeting June 18 to 20.
- About a dozen students and staff joined others from the local section of the American Nuclear Society for a tour of the San Onofre Nuclear Generation Station, General Atomics DIII-D Fusion Facility, and the USS Topeka Nuclear Submarine from August 9-11.
- The UNLV Radiochemistry Ph.D. program conducted a New Graduate Student Orientation that included presentations by the various technical subgroups on August 24.
- The Annual Report covering Academic Year 2006-2007 was completed and was distributed at the GNEP Semi-Annual Review in Phoenix, AZ, October 2-4.
- Thomas Ward visited UNLV September 10-14 to review Academic Year 2007-2008 student project proposals.

1.1 Infrastructure Augmentation

1.1.1 Infrastructure Augmentation Scope

The infrastructure augmentation component of the UNLV Transmutation Research Program enhances UNLV's research staff, facilities, and academic programs to increase the ability of the university to perform GNEP research.

1.2 International Collaboration

1.2.1 International Collaboration Scope

The international collaboration component of the UNLV Transmutation Research Program enhances UNLV's breadth of scientific and scholastic experience. University collaboration is also an efficient conduit for international collaboration that benefits the national GNEP program. UNLV has ongoing relationships with the International Science and Technology Center (ISTC) and the Khlopin Radium Institute (KRI) in St. Petersburg, Russia.

1.2.2 International Collaboration Highlights

The contract with the Khlopin Radium Institute to perform an upgrade to the UNLV Neutron Multiplicity Detector System was completed. Russian specialists are expected to visit UNLV next quarter to maintain and upgrade the NMDS.

1.3 Student Research

1.3.1 Student Research Scope

The Student Research component is the core of the UNLV Transmutation Research Program. The milestones, schedules, and deliverables of the student research projects are detailed in the individual research proposals. UNLV has 16 active student research tasks and 14 tasks that have concluded. The tasks are divided below in terms of their research area: fuels, separations, and transmutation sciences.

1.3.2 Student Research Highlights

FUELS CAMPAIGN

Interaction between Metal Fission Products and TRISO Coating Materials (Task 17) Highlights.

- Analysis continued of data obtained on the Cs/SiC samples that were investigated with Photoemission and Scanning Probe Microscopy at UNLV and with X-ray Emission Spectroscopy during the March experimental run at the Advanced Light Source, Lawrence Berkeley National Lab.
- A model was derived for the Cs/SiC interface based on the data analysis.
- Chemical cleaning experiments were performed on the SiC surfaces for the planned metal/SiC experiments.
- The graduate and undergraduate students in the project were trained at beamline 8.0 of the Advanced Light Source and performed experiments on their own.
- Analysis continued of data obtained on the Cs/HOPG samples that were previously investigated with Photoemission and Scanning Probe Microscopy at UNLV.

Dissolution, Reactor, and Environmental Behavior of ZrO_2-MgO Inert Fuel Matrix (Task 19) Highlights.

- Nitric acid dissolution studies continued on uranium-containing ceramics.
- XRD analysis on the residual powder has shown no change in phase.
- UY_6O_{12} pellets were polished to a mirror finish, so that they can be irradiated and examined by grazing angle XRD.

Design Concepts and Process Analysis for Transmuter Fuel Manufacturing (Task 22) Highlights.

- Hot Cell robot control: Continued work on the visual servoing of robots inside the hot cell. In the third quarter, visual servoing was demonstrated. For this purpose, the stereo vision system was set up in a laboratory next to a Fanuc M-16iB industrial robot.
- Sensor-Robot Integration: Driver software was written, tested and implemented for the transmission of sensor data, i.e. the target object's position and orientation, to the Fanuc robot controller.

Impact of the Synthesis Process on Structure Properties for AFCI Fuel Candidates (Task 28) Highlights.

July Monthlies

- U_2N_3 to UN reaction kinetics were obtained at three different temperatures 1000, 1050, and 1100 °C.
    - The activation energies for UN_2 to UN (424.01 kJ/mol) and U_2N_3 to UN (441.89 kJ/mol) reactions have close values supporting the UN_2 denitriding mechanism ($UN_2 \rightarrow U_2N_3 \rightarrow UN$) and the fast kinetics of UN_2 to U_2N_3 reaction.
- Two more UN_2 samples were denitridized at 675 °C under argon (5.0 grade) for 15 and 30 minutes time periods to verify the fact that there is only one phase, either UN_2 or U_2N_3, that can be detected in the 25 °C to 675 °C temperature range.
    - The UN_2 transformation to U_2N_3 is rapid so that we cannot make a sample containing both phases (Figure 1).
- A UN_2 (~ 18.0 mg) sample was dissolved in a boiling ~ 8 M HNO_3 solution and the sample is diluted 10, 100, and 1000 times to detect the fluoride levels in the sample using Ion Chromatography.
- A calibration curve is under development
    - If method is successful two samples will be examined to determined levels of F^- in UN_2
- Evaluating use of Nb metal foil to reduce formation of oxides during synthesis.
- Obtained XRD patterns of the samples of La_2O_3, ReO_2, Sm_2O_3, Eu_2O_3 mixed with excess NH_4HF_2 to check the reaction progress.
- (NH_4HF_2 + La_2O_3) : reaction is not complete yet
- (NH_4HF_2 + Re_2O_3) : reaction is not complete yet
- (NH_4HF_2 + Sm_2O_3) : reaction is complete, and the final product is NH_4SmF_4
- (NH_4HF_2 + Eu_2O_3) : reaction is complete, and the final product is NH_4EuF_4

August Monthlies

- Successfully obtained XAFS experimental time at Argonne National Laboratory for actinide nitride system
    - Experiment will be performed 17-22 October 2007
- Prepared another batch of ThNF for the $LiNH_2$ reactions.
- Nb foil was tested for use as an oxygen scavenger
    - Nb foil worked in both ammonolysis and reductions, but after ammonolysis the Nb foil tends to break into pieces.
- Kinetic examination of the (ThO_2 + NH_4HF_2) reaction was initiated and the sample examined using XRD.
    - intermediate phase of $(NH_4)_3ThF_7$ identified.

- TEM imaging on $(NH_4)_4ThF_8$ sample was collected.
- ThNF heating (at 1100 °C) under N_2-H_2 (5%) for 1 and 2 hours was also not successful in removing fluorine in the sample.
    - The 1 hour heating lead to a partial formation of $ThN_{0.90}F_{1.30}$ together with ThO_2, and 2 hours led a complete transformation into ThO_2.

September Monthlies

- Thermal behavior of ThNF studied under argon from 25°-1350°C using TG/DSC.
- TEM imaging of $(NH_4)_4ThF_8$ and NH4-U-F (4:1) samples was performed.
- Ammonolysis of (ThNF + $LiNH_2$) by ammonia and then heating under different atmospheres such as N_2-H_2 and argon lead to Th_2N_3 sample containing ThO_2 as the primary phase. A same product composition was observed for the ThNF + $LiNH_2$ reaction under other environments (Ar, Ar-H_2, N_2, and N_2-H_2). Further evaluation of reaction mechanisms for the synthesis of thorium nitrides is underway.
- Samples were prepared for XAFS experiments at Sector 12 at the APS.

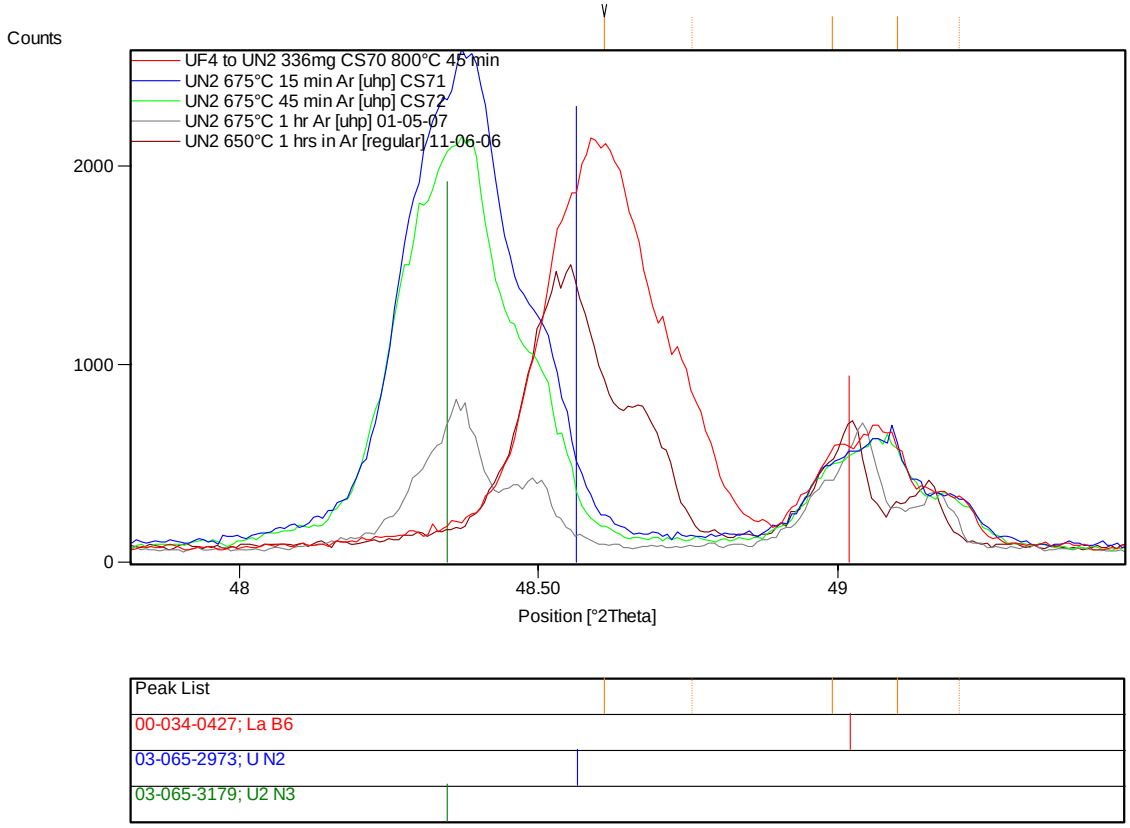

Figure 1. UN_2 denitriding reaction to form U_2N_3.

Solution-based Synthesis of Nitride Fuels (Task 34) Highlights.

- Several reactions to synthesize $UI_3(NH_3)_x$ and $U(NH_2)_3(NH_3)_x$ have taken place with limited success.

- Parameters for the cleaning of the oxide coating from U metal continued to be modified for use with liquid ammonia.
- The strategy for synthesizing the $UI_3(solv)_x$ precursor was altered to utilize the synthesis route involving THF, as reported in *Inorganic Chemistry*, with equipment, glassware, and chemicals necessary for the THF synthesis purchased.
- X-ray single crystal and powder diffractometers, necessary for identification and full characterization of the synthesized materials, were installed.

SEPARATIONS TECHNOLOGY

Immobilization of Fission Iodine (Task 15) Highlights.

- Continued to explore synthetic approaches to producing MnO_2 that would be suitable for the oxidation of iodide.
- Determined surface charge and the pH of zero charge for various samples.
- Explored the use of MnO2 to convert iodide to organic iodide.
- Performed TEM and SEM to characterize the surface morphology of various samples.

Development of Integrated Process Simulation System Model for Spent Fuel Treatment Facility Design (Task 24) Highlights.

- Completing the final version of ISOPro User Manual.
- Developed the UML diagram for software maintenance and IT documentation.

Electrochemical Separation of Curium and Americium (Task 25) Highlights.

- Presented the paper entitled, "F element studies using cyclic voltammetry in room temperature ionic liquids", 234th National Meeting, American Chemical Society**,** August 19-23, 2007. Boston, MA USA
- Continued to examine the electrochemistry of Uranium species in RTIL solutions.
- U-233 spiked Uranyl carbonate was synthesized for radiotracer quantification of species in RTIL.
- A new method for purifying RTILs using activated alumina columns yielded pure RTIL without extensive purification.

Fundamental Chemistry of U and Pu in the TBP-Dodecane-Nitric Acid System (Task 26) Highlights.

July Monthlies

- Tc-U-AHA
    - Further data workup shows that U has no discernible effect on rate of TcAHA formation as well as no effect on the final equilibrium product, previously determined by acidifying the Tc-U-AHA reactions and normalizing to LSC counts in the beta channel.

    - Examined use of AHA under acidic conditions to desorb pertechnetate from the commercially available Reillex resin, under consideration for use in the final U/Tc separations step of the UREX+ process
        - Research overlap with Tc separations and waste form studies
- TALSPEAK studies (performed by Amber Wright at ANL)
    - Extraction of Pm-147 in HDEHP at varying [NO_3^-]
        - 3 mL of aqueous phase
            - 0.1 M HNO_3
            - 0.1 μCi Pm-147
            - [NO_3^-] from 0.1–1 M
        - 1 mL of organic phase
            - 1 M HDEHP in dodecane
        - Mixed for 2 minutes
        - Let separate for 15 minutes at 25°C
        - Measured activity of each phase on LSC
    - Extraction of Pm-147 in HDEHP at varying [NO_3^-] and constant ionic strength
        - 2 mL of aqueous phase
            - 0.1 M HNO_3
            - 0.1 μCi Pm-147
            - [NO_3^-] from 0.1–1 M
            - Ionic strength adjusted to 1M with $NaClO_4$
        - 1 mL of organic phase
            - 1 M HDEHP in dodecane
        - Mixed for 2 minutes
        - Let separate for 15 minutes at 25°C
        - Measured activity of each phase on LSC
    - Both experiments gave Kex of 0.146±0.016
- Preparing manuscripts on the following
    - TcAHA/Tc-U-AHA
    - UAHA crystal structure
    - UAHA extraction
    - AHA SIT pKa

August Monthlies

- Presentation on the Uranium-TBP-nitrate system at the 234th ACS meeting in Boston, MA
- Developed manuscript on the reduction of Tc by acetohydroxamic acid (AHA)
    - Discussion with LBNL partner on reduction kinetics
- Continued analysis of uranium-AHA complexation constants with specific ion interaction theory
- Discussed development of fundamental TALSPEAK studies based on methods developed in project
- Began analysis of data to determine uranium TBP complexation constants

September Monthlies

- The effects of initial acid, pertechnetate, and acetohydroxamic acid (AHA) concentrations on the formation of *trans*-aquo technetium(II)nitrosyl diacetohydroxamate

(TcAHA) were determined; the formation of TcAHA was correlated with the decrease in TcO_4 via UV-vis spectroscopy in the perchloric system.

- The yellow-brown TcAHA complex in nitrate was titrated and the effects of pH on the UV-vis spectrum and extraction into Tributylphosphate-dodecane (30 vol% TBP) was examined; TcAHA was unextractable at all pH, and it its spectrum is independent of pH; however, deprotonated TcAHA is green, and at pH above the pKa of AHA, it decomposes to Eakins' pink complex ($Tc(II)NO(NH_3)4H_2O$).
- The effect of up to 2,000x excess uranyl (0.5 M U) on the formation of TcAHA (0.25 mM Tc) in 1 M HNO_3 and 3 M AHA was determined to be minimal; though in the absence of AHA there is no effect of uranyl concentration or time on the extraction of Tc, when uranyl exceeds two hundred-fold excess in the AHA-NO_3 system, there is a linear correlation of distribution coefficient to uranyl concentration.
- A series of AHA solutions in nitrate and perchlorate media were titrated at varying ionic strengths; the pKa values determined will be examined via SIT calculations and the pKa at zero ionic strength will be calculated.
- Literature review was done in order to plan experiments for the determination of aqueous uranylnitrato species.
- New experiments were planned to look at uranylnitrate TBP stability constants under constant ionic strength.

Investigation of Optical Spectroscopy Techniques for On-Line Materials Accountability in the Solvent Extraction Process (Task 29) Highlights.

July Monthlies

- Experimental work to evaluate the impact of iron on the absorption and fluorescence spectrum of uranium in the aqueous phase continued.
- The speciation of uranium in the organic phase of the UREX process as a function of total metal concentration was examined by UV-Vis absorbance spectroscopy. Experiments to evaluate the speciation and spectral impact of acid, nitrate, and AHA concentration on the determination of uranium in the organic stream continued.

August Monthlies

- Experiments to examine the quenching of the uranyl ion fluorescence in the aqueous phase by iron continued, focusing on additives that may be able to extend the detection of uranium in the presence of iron by laser fluorescence spectroscopy.
- The impact of nitrate concentration on the absorbance spectrum and detection limits of extracted uranium in the organic phase on was investigated covering the expected nitrate concentrations from the solvent extraction processes for the UREX and PUREX processes.

September Monthlies

- Experiments to examine the quenching of the uranyl ion fluorescence in the aqueous phase by iron continued, focusing on evaluating techniques to minimize the impact of quenching in iron-containing systems.
- The potential impact of fission products as well as corrosion products from structural materials on the absorbance spectroscopy of the actinides in process streams was explored. Based on published extinction coefficients and absorption spectra, the list of

potential interfering elements was assembled and the experimental evaluation of the impacts was prioritized.
- Experiments to examine the impact of process conditions on the ratio of peak heights for the uranyl absorbance spectrum for process monitoring and/or safeguards applications were started this month. Work this month examined the impact of nitrate concentration on the ratio of peak heights.

Combined Radiation Detection Methods for Assay of Higher Actinides in Separation Processes (Task 30) Highlights.

- Quentin Newell collaborated with Los Alamos to complete a benchmark exercise modeling the LANL Lead Slowing Down Spectrometer; Energy-time correlation constants were successfully benchmarked against the LANL model.
- Graduate research assistants Quentin Newell and Timothy Beller returned to UNLV from summer internships with Bechtel-SAIC Corp. at the Yucca Mountain Project. Their work gave them additional experience in reactor physics modeling and analysis.
- The V.G. Khlopin Radium Institute (KRI) submitted two progress reports on upgrades to add an anti-coincidence system to the Neutron Multiplicity Detector System (NMDS).
- In preparation for a visit from KRI, original Russian NMDS data acquisition system was reconnected to the detectors and initial testing to determine the status of all detectors was completed.

Synthesis and Properties of Metallic Tc and Tc-Zr Alloys as a Radioactive Storage Waste Form to Stabilize the Tc Waste Stream of the UREX+1 Process (Task 33) Highlights.

July Monthlies
- EXAFS of Tc-Zr alloys at APS with Jeff Fortner
  - Characterization of samples prepared in June 2007
- Characterization of Tc-Zr alloys by SEM, EMPA and optical microscopy.
- Sorption experiment of Tc on Reillex resin (U=200g/L, Tc=260 mg/L)
  - Evaluation of long term stability of resin for separation
- Removal of Tc from anion exchange resin by reduction with AHA
  - Based on formation of divalent Tc species
- Synthesis of Bi-Tc-O, potential waste form
  - reaction between Tc_2O_7 and dioxane (TcO_2 product)
  - disproportionation of Tc_2O_7 and TcO_2 with formation of an amorphous volatile red compound
- Submission of the Tc_2Br_8 article

August Monthlies
- Analysis of Tc-Zr EXAFS from experiments performed in July 2007
- Performed large scale sorption experiment of Tc on Reillex resin
  - 5 L scale
- Further examination of methods for removal of Tc from column with Acetohydroxamic acid
  - Results show similar results to NH_4OH solution

- Initial research on appropriate experiments for investigating dissolution mechanism of Tc waste forms

September Monthlies

- Separation U/Tc examined in a large scale experiment with solution conditions of [Tc] = 508 mg, [U] =500 g in 5.25 L 0.01 M HNO_3. The experiment examined evaporation of solution phase, separation of NH_4NO_3/NH_4TcO_4 by recipitation of (n-Bu_4N)TcO conversion (n-Bu_4N)TcO_4 to Tc metal (124.5 mg) by steam reforming. The technetium overall yield from UREX solution to Tc metal was 93 %
- Two articles were submitted: one to Radiochimica Acta entitled "Uranium/Technetium Separation for the UREX Process. Synthesis and Characterization of Solid Reprocessing Forms" and another article submitted to Journal of Coordination Chemistry entitled "XAFS spectroscopic study of $Tc_2(O_2CCH_3)_4X_2$ (X = Cl, Br)".
- The researchers attended a meeting with the CEA in Marcoule and Cadarache regarding potential transmutation studies of Tc metal. The UNLV researchers presented Tc research at UNLV.

Evaluation of Cs/Sr Waste Form for Long Term Storage and Disposal (Task 36)
Highlights.

- Feedstock materials (A36 carbon steel, 304L stainless steel, and 316L stainless steel) was received and analyzed.
- Materials compatibility coupon preparation is underway. Coupons have been cut for all three material heats and are awaiting final surface preparation.
- Bentonite clay waste former material was received and characterized (surface area, major/minor elemental composition, mineralogy).

TRANSMUTATION SCIENCES

Corrosion Mechanisms and Kinetics of Steels in Lead-Bismuth Eutectic (Task 18)
Highlights.

July Monthlies

- The Oxygen Control System (OCS) from KALLA lab (Germany) was moved from Engineering to the High Temperature Materials Laboratory (CHE 112C), and put into operation.
- Raman analysis and instrumentation improved and data were taken on metallographic cross sections.
- Gas phase experiments progressed.
- Community involvement via NSF Research Experience for Undergraduates (REU) program and a local high school student volunteer.

August Monthlies

- Physics graduate student Dan Koury finished the first draft of his doctoral dissertation with expected graduation in December 2007.
- Significant maintenance on the XPS machine to address 3 week long downtime was done.

- Reference Raman spectra of well-characterized spinels were obtained and compared with literature and experimental values.
- Comparisons of gas-phase and LBE corrosion of steel continue to yield insights into corrosion mechanisms, including an unexpected reduced iron species in some cases.

September Monthlies

- Dan Koury continued writing his doctoral dissertation, and is expected to graduate with his Ph. D. in December 2007.
- Brian Hosterman obtained standards of chromium-containing spinels, which will be very useful in identifying Raman spectra of compounds created during corrosion of steel.
- Thao Ho took the first data using the residual gas analyzer (RGA), for direct monitoring of the composition of the gas-phase constituents.
- Initiated training in SEM operations to transfer expertise in SEM operations from Dan Koury, expected to graduate in December 2007.

Impact of Silicon on Corrosion Resistance of Stainless Steels in LBE Systems (Task 20)
Highlights.

- The results of SSR testing of T91 grade steels performed under controlled cathodic (negative) potentials revealed reduced failure strain (e_f), percent elongation (%El), percent reduction in area (%RA), time to failure (TTF) and true failure stress (σ_f).
- The extent of such reduction was more pronounced at higher temperatures under more cathodic applied potentials indicating greater cracking susceptibility (Figures 22 and 23).
- The increased cracking tendency of the tested materials under more negative applied potentials at 30 and 60°C may be attributed to the generation and entrapment of hydrogen within their matrix. However, at higher temperature (90°C), hydrogen might have permeated through the matrix of the tested materials, indicating insignificant effect of controlled potential on the cracking tendency. No detrimental effect of anodic applied potential was seen irrespective of the Si content and temperature.
- The results of tensile testing of T91 grade steels of varied Si content, performed at strain rates of 10^{-2}, 10^{-3}, and 10^{-4} sec^{-1}, revealed a minimum failure strain at 400°C similar to the testing conducted at $5x10^{-4}$ sec^{-1} (Table 3). Simultaneously, the occurrence of serrations in the engineering stress versus engineering strain (s-e) diagrams was more pronounced in steels with higher Si content at a strain-rate of 10^{-4} sec^{-1}. These results suggest that the diffusivity of solute elements was higher at the slowest strain-rate due to the longer deformation times.
- The charpy test was quite useful in evaluating the role of Si content on the amount of energy absorbed prior to the fracture of rectangular specimens containing a V-notch. These results indicate that the presence of higher Si content in T91 grade steels resulted in reduced impact energy and higher DBTT temperature, indicating reduced impact resistance. The variation of impact energy with temperature, and the overall charpy testing data are shown in Figure 24 and Table 4, respectively.
- The results of localized corrosion studies involving 12Cr-1Mo steels indicate that the magnitude of E_{corr} became more active (negative) with increasing temperature, irrespective of the Si content (Figure 25). A similar effect of temperature on E_{corr} has been reported in numerous investigations performed earlier.

Oxide Film Growth Modeling in LBE Systems (Task 21) Highlights.

- The post processing on the numerical data from cellular automaton (CA) modeling on the oxidation process coupled with inward oxygen transport along the grain boundaries was finished and the results have been analyzed.
- A revised journal paper on the oxide layer growth model using CA method at a mesoscopic level was submitted to *Computational Materials Science* in August 2007. A few references and supplementary materials have been added in order to increase the quality of the paper based on the editor's suggestion. This journal paper has been recommended to be published by the reviewers. The final review on the revised version of paper is in progress.

  Taide Tan, Yitung Chen, and Huajun Chen, "An Improved Mesoscopic Oxidation Model of Metals in Lead Bismuth Eutectic," *Computational Materials Science,* revised version submitted.
- One conference proceeding abstract based on the CA model has been submitted to the Sixteenth International Conference on Nuclear Engineering (ICONE 16).

  Taide Tan, Yitung Chen, and Huajun Chen, "Simulations of Metal Oxidation in LBE at a Mesoscopic Level," ICONE16-48025, May 11-15, 2008, Orlando, Florida, USA.
- More literature surveys have been conducted on the oxidation process of metals. The benchmark of the diffusion-controlling oxidation model considering the scale removal effect on the thicknesses of the inner oxide layer and outer oxide layer for stainless steel in lead-bismuth eutectic (LBE) has been finished.
- One conference proceeding has been accepted to be presented and published in 2007 ASME International Mechanical Engineering Congress and Exposition.

  Taide Tan, Yitung Chen, and Huajun Chen, "Modeling of a Diffusion Controlling Oxidation Process with Scale Removal in Oxygen-containing Liquid Flow," IMECE2007, Nov 11-15, 2007, Seattle, WA.
- The Embedded Atom Method (EAM) of molecular dynamics (MD) model has been successfully implemented into the Moldy program. A few test runs were performed and the results appear to be reasonable. The system in the test runs is a semi-infinite aluminum slab (12 A thick). The total energy with the Lennard-Jones potential is about 1000 J, while the total energy with the EAM potential is about 500 J. Both results are in the same order of magnitude.
- The variable charge model was also implemented. A test run shows a superior result over the old fixed charge model. The test system is composed of a semi-infinite aluminum slab sandwiched between two layers of oxygen gas, one on each side. The old fixed charge model shows that oxygen gas bounces around on the material surface without any sign of oxidation. Aluminum is used in the numerical model study first to validate it with the available data from publications. The oxygen interaction in the fixed charge model is purely due to the Lennard-Jones potential, and there is no Coulomb force involved because the net charge in the aluminum slab must initially be zero. On the other hand, the EAM potential coupled with the variable charge model offers a promising sign of oxidation. The aluminum atoms in the slabs rush out to oxygen molecules, and hence the slab expands and becomes virtually porous.

Corrosion Barrier Development for LBE Corrosion Resistance (Task 23) Highlights.

September Monthlies

- Nanowires created by electrophoretic deposition of nanoparticles were characterized using field emission scanning electron microscopy
- To improve the nanowire material, a second batch of nanowires were created using sonication during electrophoretic deposition
- The samples were annealed in the oven and are being characterized for material quality

Reactor Physics Studies for the AFCI RACE Project (Reactor-Accelerator Coupling Experiments Project (Task 27) Highlights.

July Monthlies

- As General Chair, the PI continued to plan for the Eighth International Topical Meeting on Nuclear Applications and Utilization of Accelerators (AccApp'07), a joint ANS-IAEA meeting. The meeting was held July 30 to Aug. 2 at Idaho State University (home of the nation's largest academic accelerator laboratory) in Pocatello, Idaho.
- UNLV doctoral student Evgeny Stankovskiy reported the results of his research and participated in other discussions at the Eighth International Topical Meeting on Nuclear Applications and Utilization of Accelerators (AccApp'07).
- UNLV M.S. in N.E. students Timothy Beller and Ryan LeCounte prepared a poster, presentations, and three full papers on their high-power target for AccApp'07. The PI presented the poster and oral presentations.

August Monthlies

- The UNLV RACE Project was completed the end of August. A final report is in progress.
- UNLV doctoral student Evgeny Stankovskiy is continuing to use MCNP to analyze delayed neutron physics in RACE-ECATS experiments as he completes his doctoral dissertation.
- As General Chair, the PI wrapped up a very successful Eighth International Topical Meeting on Nuclear Applications and Utilization of Accelerators (AccApp'07), a joint ANS-IAEA meeting. The meeting was held July 30 to Aug. 2 at Idaho State University (home of the nation's largest academic accelerator laboratory) in Pocatello, Idaho.

Decoupling and Disturbance Rejection Control for Target Circulation (Task 31) Highlights.

July Monthlies

- One conference paper was sorted out and submitted to the AccApp 07 conference.
- Master student, Xiuju Tan, went to the above mentioned conference.
- The power supply for the by-pass heater control system was installed.
- A variable frequency driver was installed for the EM pump testing.

August Monthlies

- Secondary cooling systems with compressed air (for the Heat exchanger) and water (for the radiation shield) were installed to remove heat generated by the Electromagnetic pump.
- Graduate student Julia Tan started to write a thesis for her Master degree.

- The TC-1 was remodeled according to its original design drawing using SolidWorks for further modification.

September Monthlies

- The graduate student continued writing their Masters Thesis

Magnetohydrodynamic Simulation of Electromagnetic Pump in TC-1 (Task 32) Highlights.

- An online database of articles and papers related to EM pump technology has been created. Wiki-based software is being used to reorganize the papers in this database in order to expand the potential for greater collaboration amongst the various project researchers.
- Work has started on using the commercial CFD package Fluent as the core of the coupled magnetohydrodynamic (MHD) solver for use in design and optimization of new EM induction pumps.

Criticality Studies for UREX Processes (Task 35) Hightlights.

- Graduate research assistant Larry Lakeotes returned to UNLV from a summer internship with NSTec (National Security Technologies, LLC) at the Remote Sensing Laboratory of the Nevada Test Site.
- Graduate research assistant Ryan LeCounte returned from a summer internship with Bechtel-SAIC Corp. at the Yucca Mountain Project, which gave him additional experience in reactor physics.
- The NJOY99 cross section processing code, which was acquired and installed for use with other code systems in sensitivity studies, required modification before use to create cross section libraries for sensitivity studies.

Deep Burn Separations and Repository Behavior Highlights.

July Monthlies

- Further Beta-SiC sorption studies for TRISO repository behavior
    - Continuation of sorption experiments on β-SiC for pH 4-10 experiments, initiating second round of experiments
        - Verification and utilization of Micro pH probe and ORP for assessing Eh and pH
        - New ORP and microelectrode calibrated
    - Refinement of desorption study methodology
- Development of cloud point separation presentation for American Chemical Society Meeting in August
- Publication on fluoride based synthesis of uranium nitride, involving the treatment of UO_2 by NH_4FHF, in Journal of Nuclear Materials

August Monthlies

- Alpha Spectrometer for solution phase analysis
    - 8 new chambers installed and tested
    - Software migration from Windows 98 operating system to Windows XP operating system completed

    - 12 chambers calibrated, system is fully functional
- Electroplater for preparation of alpha spectroscopy samples
    - 6 sample holders constructed
    - Electroplater tested and fully functional
- Data collection continued for second round of Beta-SiC sorption/desorption experiments
    - Focus on kinetics of desorption
- Prepared and presented at Boston ACS meeting "Curium Separation from Europium by Cloud Point Extraction using 8-Hydroxyquinoline"

September Monthlies

- Alpha Spectrometer
    - Thirty two polyethylene plates were machined to replace the stainless steel sample holders provided with the chambers. The polyethylene plates are easier to clean, and utilize a lipped, disposable steel planchet as contamination barrier. The use of the new sample holders result in reduced background count rates, less cross contamination from high activity samples and require less maintenance than the OEM holder.
- Second generation column vacuum box
    - Construction of the 3x5 vacuum box (15 samples) is nearly complete. All of the machining and assembly have been completed; the new cover seal based on a flowable silicone material has to be tested.
- Beta-SiC sorption/desorption experiments
    - Sorption experiments running at pH 3, 5, 5.65, 7 and 9 have been continued through 1056 hours. These systems appear to be at or near equilibrium
- Hot Particle – Elemental Mapping Experiment
    - Hot particle 10-F-7-D, containing plutonium, americium and gallium, was prepared for an elemental mapping experiment (Pu, Am, Ga) at ANL/APS scheduled for 14-Oct-2007.
- Distribution and separation factors were calculated from previous cloud point extraction runs and data were combined with all data ever collected for cloud point for comparison. There appears to be some systematic error between individuals performing the experiment. Source of systematic error is unidentified.
- Molar abosrptivities for Triton X-114 were measured at 224 nm and 277 nm absorption peaks in preparation for the sequential extraction experiment.
- Presentation on recent work at PNNL was prepared and delivered at the Office of Civilian Radioactive Waste Management Fellowship Workshop in Las Vegas on September 25, 2007.

FUELS TECHNOLOGY

Interaction between Metal Fission Products and TRISO Coating Materials (Task 17).

The focus in this quarter was on the analysis of the XPS, UPS, XES, and AFM data sets collected during the last two quarters. These datasets consist of two Cs thickness series, one on HOPG and one on SiC. Both surfaces were thoroughly cleaned ex-situ by cleaving (HOPG) and HF etching (SiC) as well as in-situ by heating of the substrate for the desorption of adsorbates (SiC).

The XPS survey spectra for different Cs evaporation times (and hence different Cs film thicknesses) on SiC are shown (Figure 2). In the presented case, a C-terminated 6H-SiC(0001) single crystal surface was used. After Cs evaporation, all expected Cs lines can be found in the spectra. The intensity of these lines, which can be related to the amount of Cs deposited, increases for increasing deposition time (as expected). In parallel, the lines of the SiC substrate, namely C 1s, Si 2s, and Si 2p, slightly decrease in intensity. Similar to the Cs/HOPG case presented in the last quarterly report, the decrease of the substrate line intensities is considerably smaller than expected from the strong increase of the intensities of the Cs lines. This finding suggests that the deposited Cs forms islands leaving parts of the substrate uncovered, rather than a homogeneous film.

This qualitative finding is supported by a thorough analysis of the Cs $3d_{3/2}$, Si 2p, and C 1s detail spectra. Both the Cs $3d_{3/2}$ and Si 2p spectra show one dominant component (chemical species) and no change in spectral shape after Cs deposition (not shown). In contrast, the C 1s line shows two different chemical species for the pure SiC substrate and a strong change (i.e., the emergence of a third species) after Cs deposition, as can be seen in Figure 3. Besides the experimental data, shown as circles, Figure 3 shows a detailed peak-fitting analysis performed by the graduate student. All spectra were fitted simultaneously, keeping the peak widths for each component and the distances between the different components constant throughout the whole thickness series.

The finding of three different carbon species can be understood as follows: Since the given SiC surface is C-terminated, two chemical carbon components (labeled A and B in Figure 3) are present. While component A can be attributed to carbon in a fully coordinated SiC environment (i.e. the bulk carbon species), component B represents the surface-terminating carbon layer, hence called the surface carbon species. In contrast, for a carbon-terminated SiC, all Si atoms will be in a fully-coordinated environment and therefore only one Si species exists. After Cs deposition, a third carbon species (labeled C) can be found. This third species can be attributed to surface carbon atoms that are now also bound to the deposited Cs atoms (i.e., this species represents an interface species).

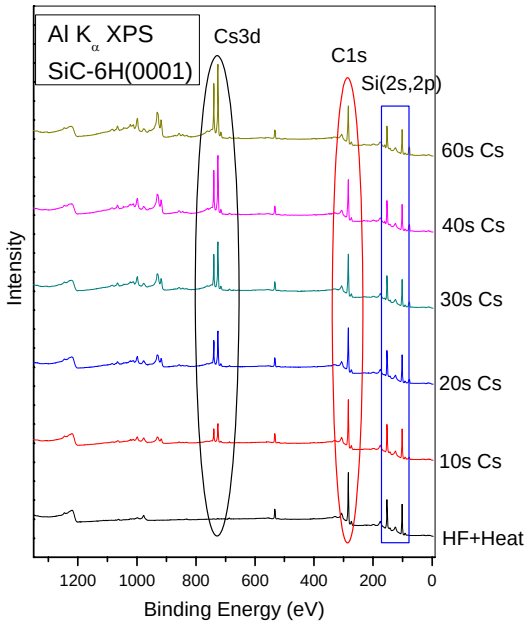

Figure 2. XPS survey spectra of an SiC substrate after etching and heating as well as after stepwise deposition of Cs.

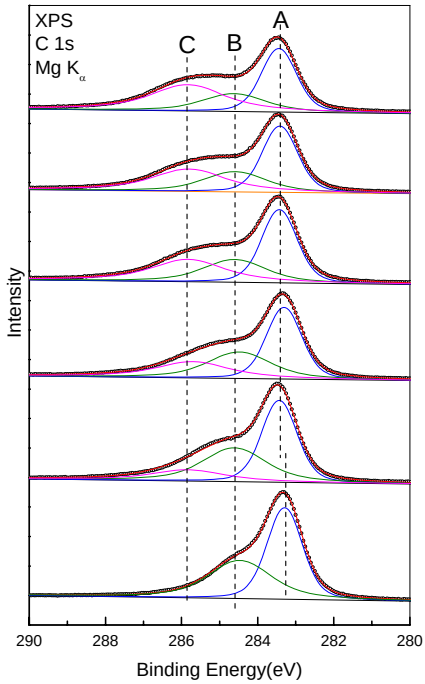

Figure 3. C 1s detailed spectra and corresponding peak fit analysis. Experimental data points are show as circles, colored lines show the different fitted peaks.

The fractions of the three different carbon components is shown as a function of Cs deposition time (Figure 4). While the fractions of the bulk and surface species (A and B) decrease, the interface species strongly increases in weight, as expected.

For a more detailed investigation of the Cs/SiC growth morphology, AFM and STM experiments are planned.

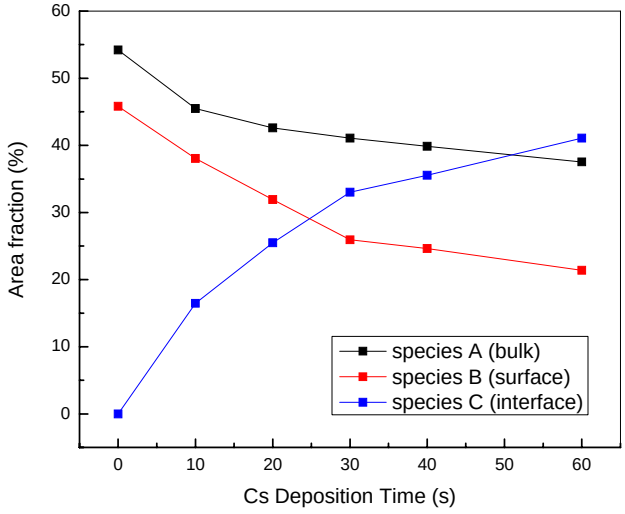

Figure 4. Area fraction of the different carbon species as a function of Cs deposition time.

Dissolution, Reactor, and Environmental Behavior of ZrO_2-MgO Inert Fuel Matrix (Task 19).

Dissolution studies

Nitric acid dissolution studies on uranium containing ceramics were continued in the current quarter. A linear dissolution was observed. Two experiments have been performed on the composition with 75% (wt/wt) MgO with concentrated HNO_3. Further experiments need to be performed to determine the rate of the dissolution. A new experimental procedure has been developed to run three experiments simultaneously, which has allowed for more consistent data in other experiments and will assist in determining the rate constants for the dissolution. The resulting rate constants for the examined ceramics (see figure below) are 0.0012 mM U/m^2/hr for $Zr_{0.325}Mg_{0.6}U_{0.05}Er_{0.025}O_{1.39}$ and 0.0342 mM U/m^2/hr for $Zr_{0.175}Mg_{0.75}$ $U_{0.05}Er_{0.025}O_{1.124.}$ The trend supports higher dissolution with higher Mg levels and will be verified in future studies.

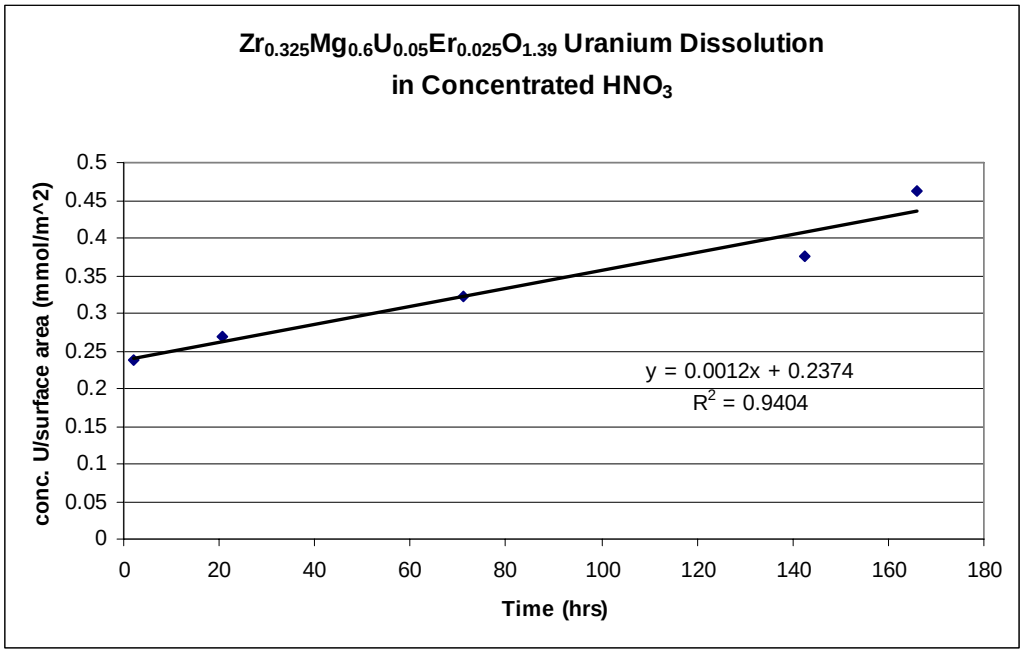

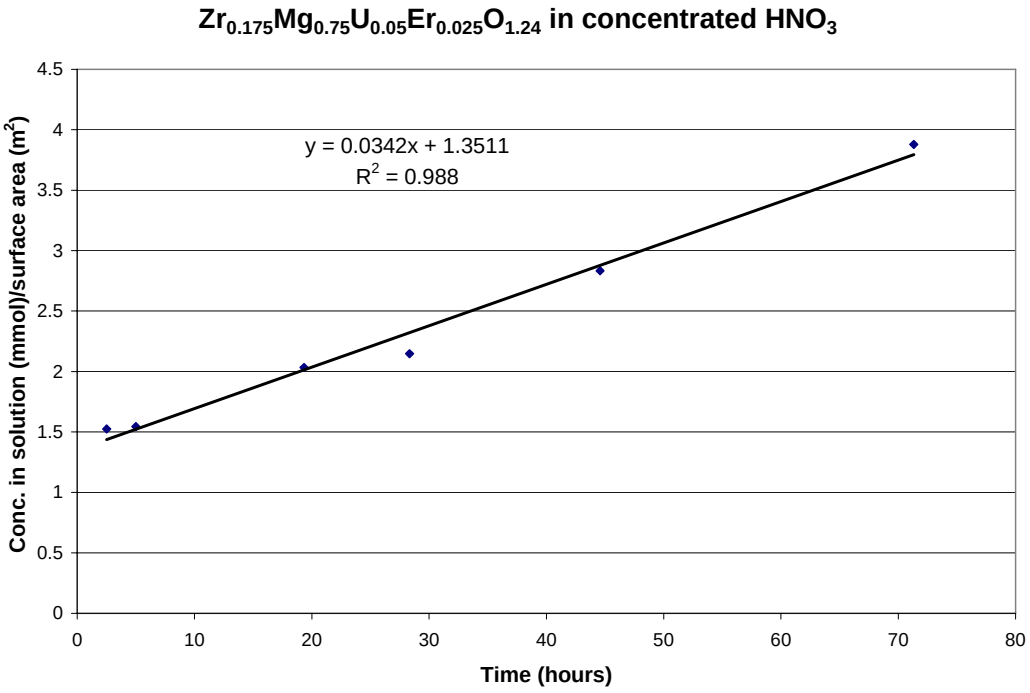

XRD analysis

XRD analysis on the residual powder has shown no change in phase. Pellets containing 60% (wt/wt) MgO show kinetics an order of magnitude slower than the 75% (wt/wt) MgO composition. Dilute (1 M) HNO_3 proved to be insufficient to leach any significant quantity of the uranium out of the pellet, even at MgO contents as high as 75% (wt/wt).

Waste form studies

UY_6O_{12} pellets were polished to a mirror finish, so that they can be irradiated and examined by grazing angle XRD. The material was also characterized by SEM, microprobe, XRD, optical microscopy, and TEM. The material was found to be a single phase of UY_6O_{12}. $U_2Y_6O_{15}$ was synthesized and sent to Los Alamos National Lab for irradiation. ULa_6O_{12} was synthesized; however, forming a dense pellet that is still under investigation.

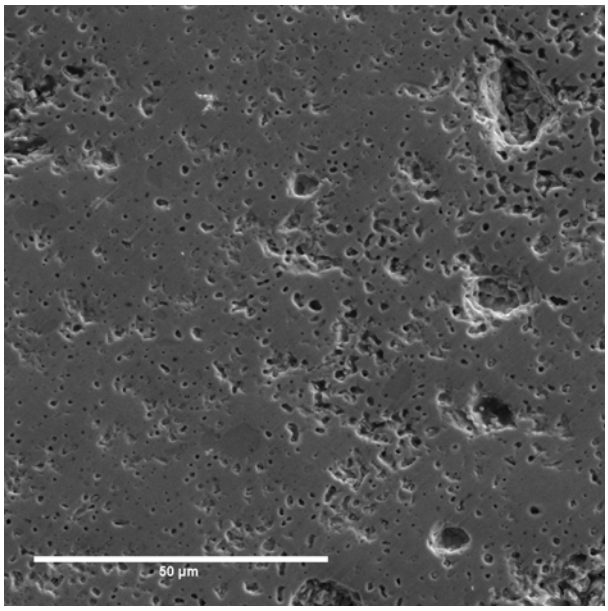

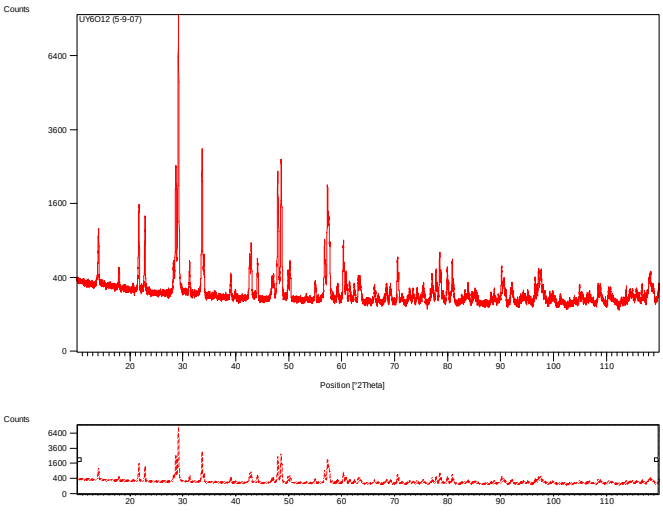

Collaborations

Experiments were performed with $Zr_2Nd_2O_7$-MgO from Univ. of Florida in concentrated H_2SO_4. Nd and Mg follow first order kinetics. Three experiments were performed under parallel conditions. Results are shown in the graphs below. The resulting 1st order rate constants for the

elemental dissolutions were found to be 0.0310±0.0025 hr^{-1} for Mg and 0.0297±0.0020 hr^{-1} for Nd, indicating congruent dissolution for the material.

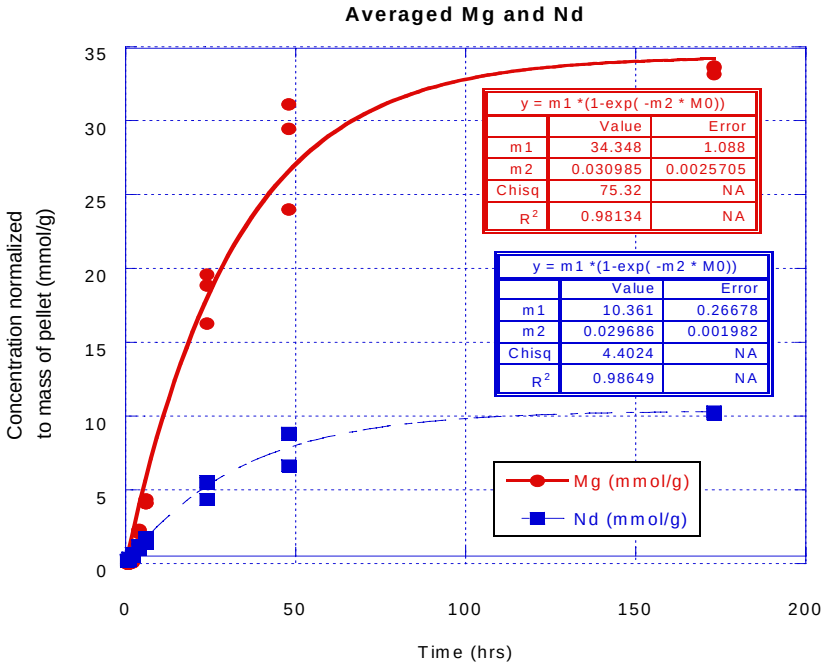

Design Concepts and Process Analysis for Transmuter Fuel Manufacturing (Task 22).

Accelerated Object Extraction

The contour extraction algorithm can require long durations during image feature extraction (Canny Edge Detection, up to one second per image). Since the cylindrical targets each cover only a portion of the image, there is no need to apply the feature extraction to the whole image. By fragmenting each image into sub-images containing the desired objects, the duration of the feature extraction can be significantly reduced (Figure 5).

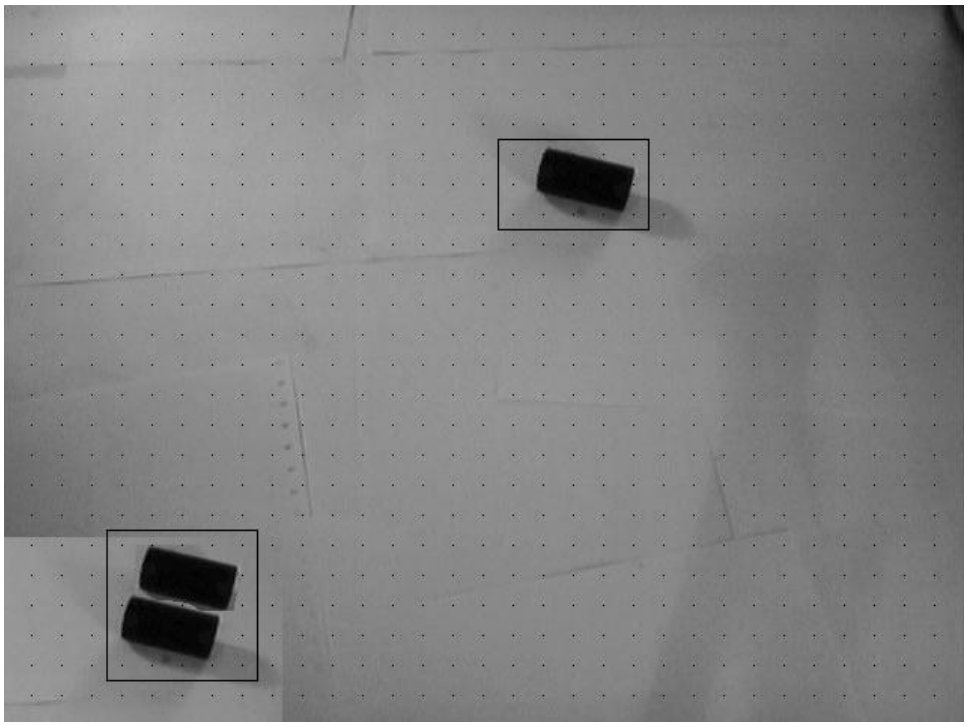

Figure 5. Finding the regions containing the targets by undersampling - The black spots represent the sample points, the black rectangles are associated with the extracted regions.

Targets are found by undersampling the image and testing the neighborhood of the respective pixels for their color. In this application black pellets are being searched for (i.e. for black pixels in the neighborhood). By merging all black neighboring locations, the rectangular boundaries of the pellets can be determined by ascertaining their respective contours. To avoid corners of targets in certain angles not being collected by the sampling and possibly being eliminated, the search algorithm doubles the number of search points at each of the four sides. The duration of the edge detection process depends on the number of objects in the scene, but is usually a fraction of the amount a complete detailed search.

Steering & Rotation of the Robot End Effector, Gripping Operations

For gripping horizontal cylindrical targets, the orientation of the cylinder is required. The orientation can easily be computed as the angle between the two extracted surface points and the x-axis. To align the gripper with the target's orientation, the last joint of the robot has to be rotated. For this purpose, the orientation of the cylinder in the bin (in world coordinates) is transformed to robot-specific joint coordinates (Figure 6).

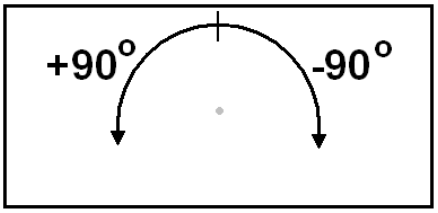

Figure 6. Gripper rotation parameter - Angle between 90 and -90 degree.

After accomplishing the process of picking up targets with a given position and orientation, the first autonomous tests were conducted. In these tests a single target was randomly placed in the scene, picked up by the robot, and dropped in a box (Figure 7). In later test scenarios, the robot placed the target at randomly generated positions and picked it up again. This procedure was tested iteratively.

Figure 7. Robot grasping a cylindrical pellet.

Multiple Objects

To extract multiple objects, the existing algorithm, which so far extracted only the coordinates of one object, was extended. The extended algorithm returns a list of point n-tuples representing the two cylinder surface points for each identified target in the corresponding image. When these lists are created for each of the stereo image pairs, the correspondence matching between targets in both lists is performed using epipolar geometry.

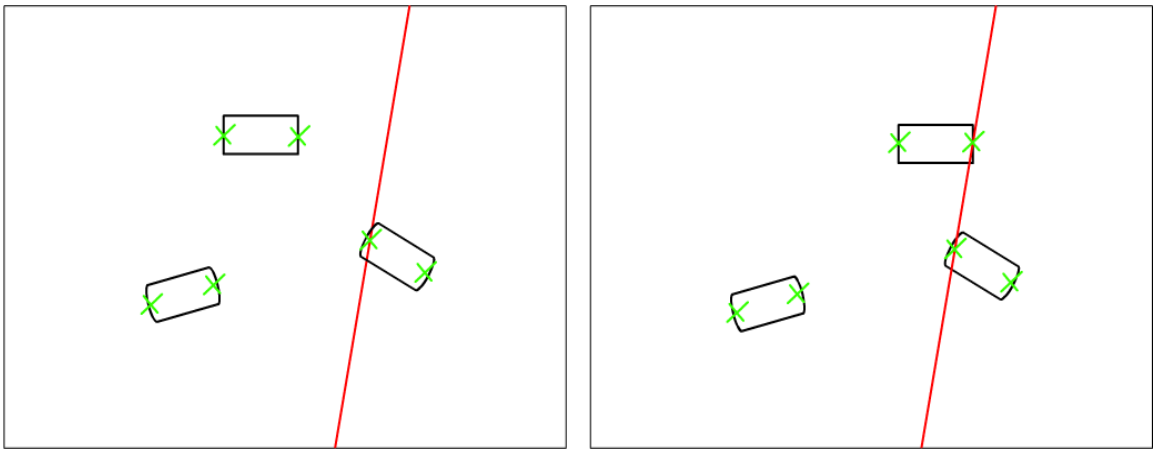

Figure 8. Finding correspondences between targets with the epipolar geometry.

In Figure 8, the left image shows the epipolar line (red) for a corresponding point that was selected in the other stereo image. Here, the corresponding point is found as the point that lies on (or close to) the epipolar line. A less trivial case is shown in the right image (Figure 8). The

epipolar line intersects two possible points (targets) that may correspond with the selected target. Here, the epipolar geometry fails to find unique correspondences.

To organize the search for correspondences uniquely, additional information may have to be included. These could be the locations of the image edges; for example, the bottom of the first image matches with the top of the second image.

Upright and Horizontal Targets

In general, there is no need to differentiate between upright and horizontal objects during the target extraction phase. The objects' orientations have no bearing on the appearance of the cylinder in the image, usually the mantle and one end surface (Figure 9).

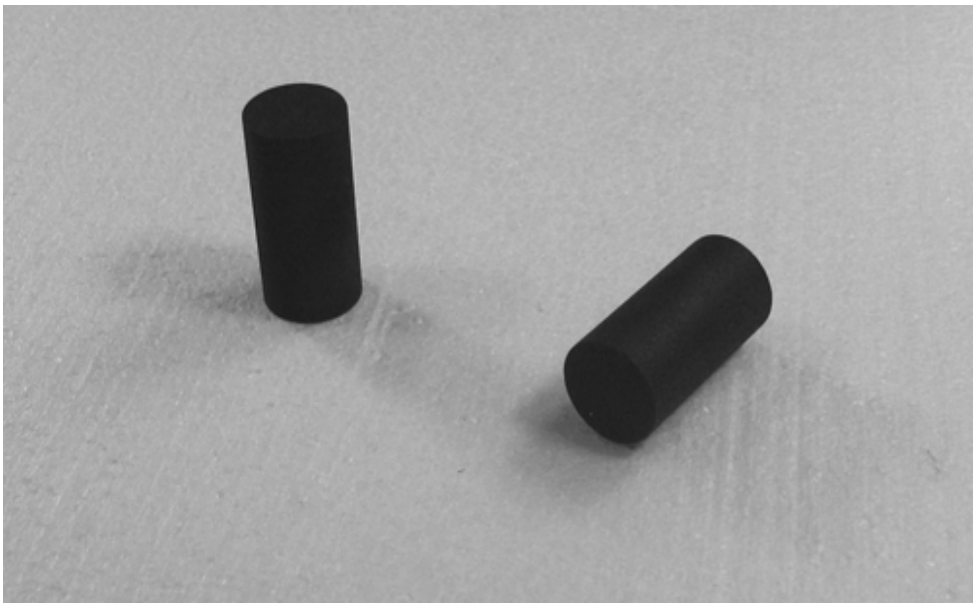

Figure 9. Upright and horizontal targets.

The determination of a cylinder's orientation is made after the two surface end points of each detected object (Figure 7) have been triangulated. If the resulting 3D points are located at the same vertical elevation, the object is horizontal. Otherwise a standing object is assumed.

Graphical User Interface

After the completion of the basic operations for cylinder grasping a demonstration application was developed. The program offers a graphical map of the scene contents (such as position and orientation of the objects), and tracks the manipulation of single objects (Figure 10). To perform picking and placing of targets, the user selects a specific target by mouse click in order to have the robot execute a set of user-defined operations.

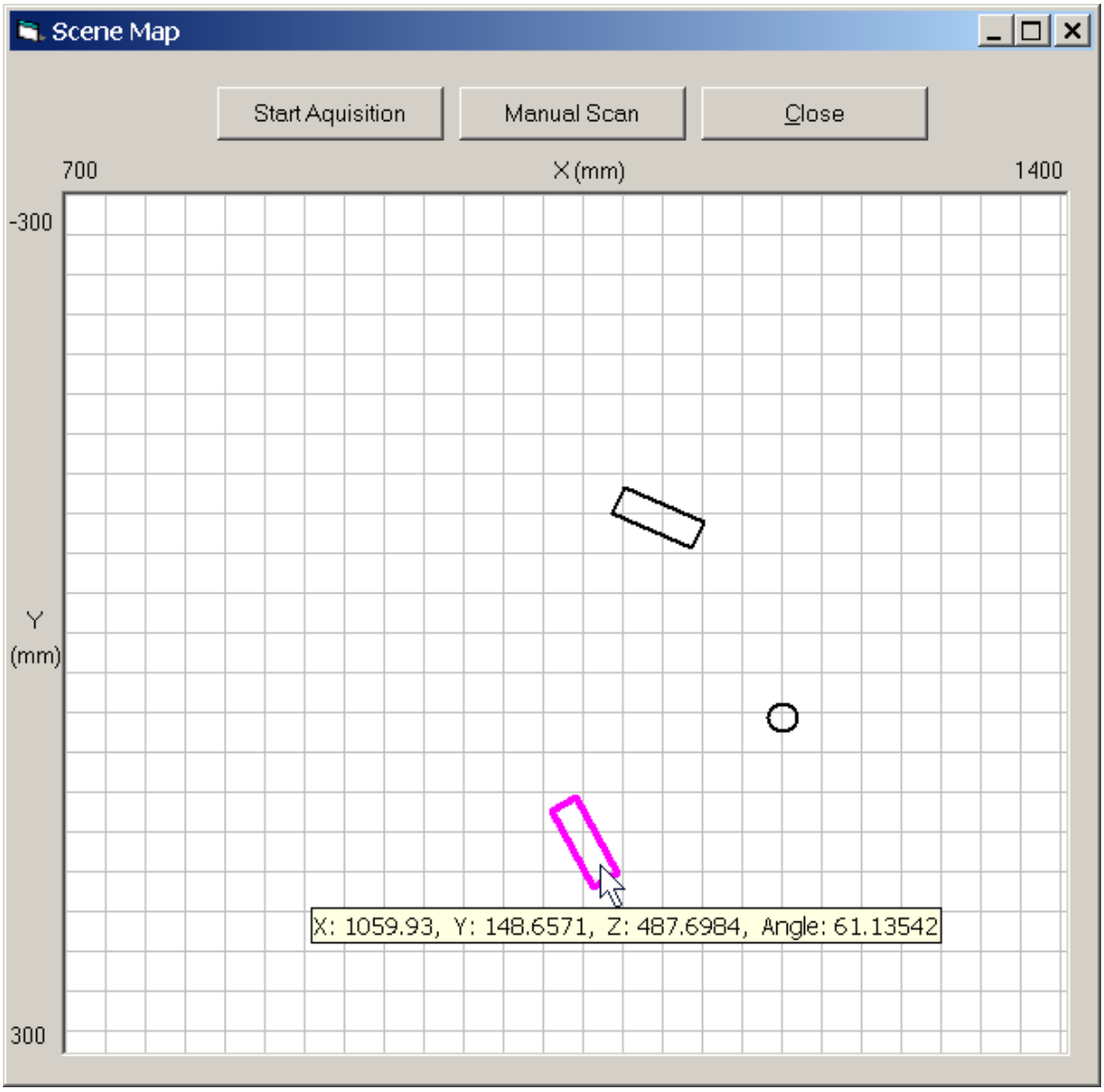

Figure 10. Screenshot of Graphical User Interface (GUI) for Robot control. Here, the user has selected the object at the bottom of the image for grasping. The controller software highlights the selected object and displays its coordinates and angle of orientation. The object to the right of the selected one is oriented upright.

Impact of the Synthesis Process on Structure Properties for AFCI Fuel Candidates (Task 28).

Solution-based Synthesis of Nitride Fuels (Task 34).

One of the original synthetic routes devised for the synthesis of U(III)N involved the entire reaction taking place in liquid ammonia. Several experimental reactions were conducted in an attempt to synthesize the $UI_3(NH_3)_x$ and $U(NH_2)_3(NH_3)_x$ precursors of U(III)N. Each attempt was involved cleaning of the uranium metal to remove the oxide coating of the metal reagent

with 3 washes of concentrated nitric acid, each followed by a rinse with liquid ammonia. Success of this cleaning procedure was varied, with a majority of cleaned metal oxidizing rapidly once in contact with the liquid ammonia, despite the precautions taken to eliminate oxygen contamination in the reaction flasks. Due to the continual presence of oxide coating of the uranium metal, it was decided to alter the proposed synthetic route to utilize the synthesis of the $UI_3(THF)_4$ precursor, as described in *Inorganic Chemistry*. This involves the purification of THF through distillation, cleaning of the metal uranium, and slow reaction of U and I_2. Equipment to perform this synthesis was not available for immediate use, but all necessary glassware was purchased.

It was discovered that the uranium metal turnings being used for the synthesis had a possibility of containing niobium as well. Waste solutions were analyzed by ICP-AES, and no niobium was identified. Other reaction waste solutions were also analyzed in order to determine the reactivity of uranium in the liquid ammonia solution. These analyses determined that only a minimal amount of uranium became dissolved, indicating that either there was little reactivity in the liquid ammonia or the reaction was only taking place on the surface of the metal. Neither of these possibilities is desirable, therefore the synthetic route involving THF was selected to avoid these outcomes.

Single crystal and powder diffractometers are necessary instruments for the determination of the intermediate and final products. Single crystal diffraction will be used in order to determine the structure of larger single crystal samples obtained during the reaction. Powder diffraction is needed to identify the purity of the yields after each step of the reaction process. After the purchase of these instruments (purchased on a non-TRP account), two former offices were prepared for the installation of these instruments. Additional electrical lines, plumbing fixtures and piping were installed, because of the requirements of the diffractometers. These instruments were installed, with training obtained by the personnel involved with Task 34.

SEPARATIONS TECHNOLOGY

Immobilization of Fission Iodine (Task 15).

This task continued to perform iodide oxidation experiments with various manganese oxide experiments. In the last round of experiments, 4-hydroxybenzoic acid, or Vanillic Acid, were included in the reaction mixture in order to trap iodine in an organic form. Experiments were performed at pH 4 and 6 with Manganese Oxide (VIP 57). The reaction mixtures were analyzed by reversed phase HPLC. Chromatographic separation of reaction products was performed with an acetonitrile-acetic acid (0.05M) gradient. Chromatograms were recorded at 280 nm. At pH 4, both vanillic and 4-hydroxy benzoic acid reduced the manganese oxide and only trace quantities of iodinated organic products were apparent. At pH 6, the oxidation of 4-hydroxybenzoic acid by manganese oxides were much slower and two iodinated products were apparent. These products have been identified as 3-iodo-4-hydroxybenzoic acid and 3,5-diiodo-4-hydroxybenzoic acid. A series of chromatograms where starting material and products are identified is shown in Figure 11. The reaction occurred at room temperature. The reaction mixtures were allowed to proceed for 24 hours, before they were filtered and analyzed by HPLC as described above. The formation of iodinated products was proportional to the iodide concentration in the reaction

mixture; however, the extent of iodide conversion under these conditions was less than 10%. Similar experiments with vanillic acid demonstrated that vanillic acid was oxidized under these conditions, thus preventing the formation of iodinated byproducts.

Because the rate of iodide oxidation is much higher at low pH, and the rate of iodine reaction with phenolics is higher at high pH were decided to try to segregate the reactions in order to maximize sequestration. Potassium iodide standards were mixed with a γ-MnO_2 (0.1 g) and 50 mL of distilled water. The mixture was acidified with 0.2 mL of 12N HCl. The mixture was allowed to react for about 10 minutes and then filtered (through a glass fiber filter) into a flask containing 0.01 moles of $NaHCO_3$ and 300µmol of vanillic acid in 50 mL of water. The reaction mixture was analyzed for free iodide using a specific iodide electrode and then for iodovanillic acid by HPLC. The results of the analysis indicated that 50% of the iodide was converted to iodovanillic. This is consistent with the γ-MnO_2 oxidizing the iodide to molecular (I_2) that could be converted to organic iodide by aromatic substitution. The results from this experiment are shown in Figure 12.

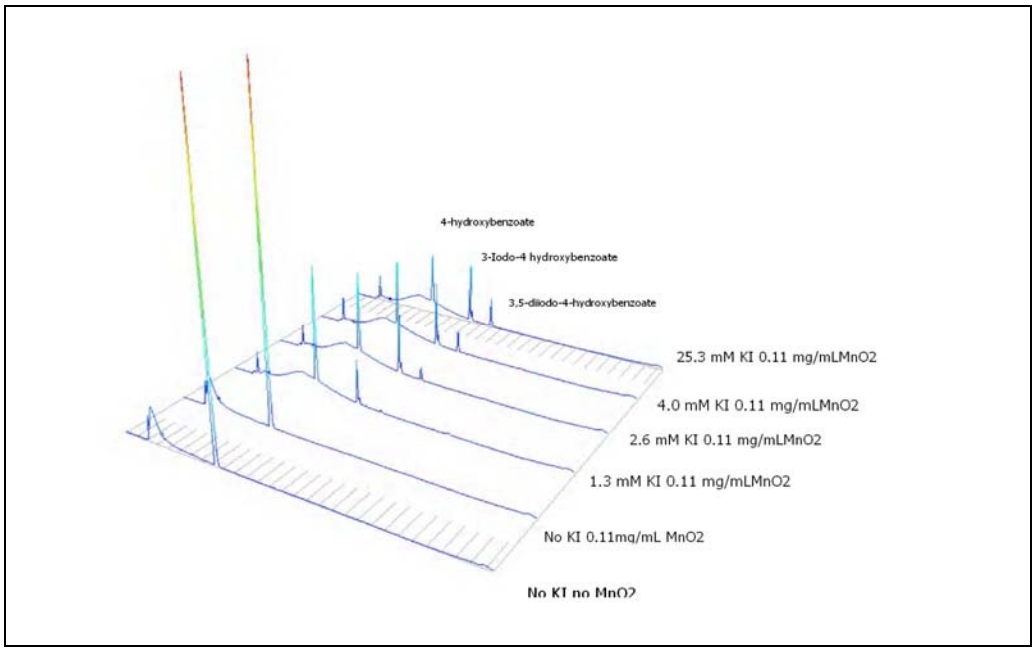

Figure 11. Iodination of 4-hydroxybenzoic acid by manganese oxide at pH 6. The reaction was allowed to proceed for 24 hours at room temperature before analysis.

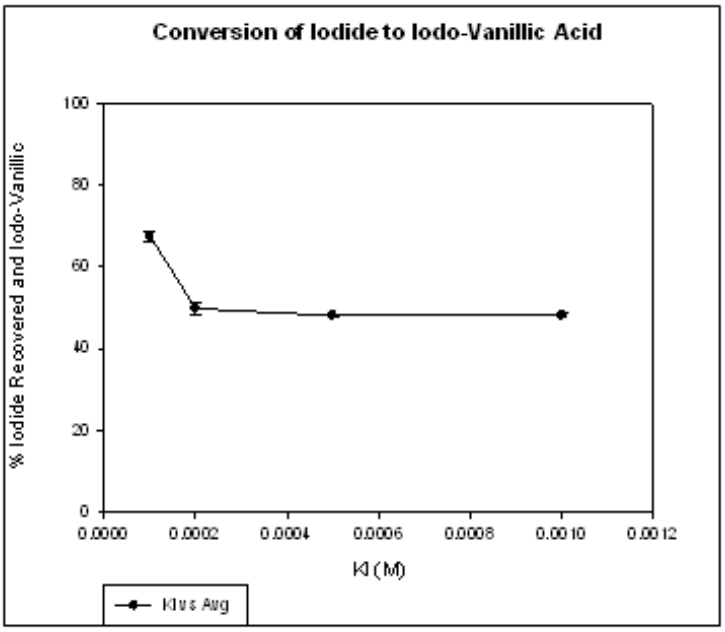

Figure 12. Conversion of iodide (at various concentrations) to iodovanillic acid using a binary MnO_2 oxidation process.

Development of Integrated Process Simulation System Model for Spent Fuel Treatment Facility Design (Task 24).

Completing the final version of ISOPro User Manual

- Added information and updated section 7.1.1 – detailed elements for AMUSE.
- Updated descriptions for screen shot in section 4 - Basic Steps of Running ISOPro.
- Appendix A documents all modules from the ISOPro package that provide hyperlinks to the source codes listed in Appendix B.
- Final version of the ISOPro User Manual will have summarized ISOPro source codes in Appendix B.

Set up Unified Modeling Language (UML) diagrams for the ISOPro project (User Guide for IT professional)

- To better maintain and improve the ISOPro system engineering package, construction of Unified Modeling Language (UML) diagrams are in progress. Those diagrams provide high flexibility on version control, code comparison and module modification. They can be distributed to different development identities in the future for coordinating software improvement and modification effort. There are three major components under development:
    - Class Diagram for AMUSE middleware interface as show in Figure 13.
    - Class Diagram for ASPEN-Plus middleware interface.
    - Use Case for ISOPro package.

- Unlike the general user manual or tutorial development in Section 1, the UML diagrams provide current and future programmers/software engineers a clear module definition and data flow of the software as shown in Figure 14.

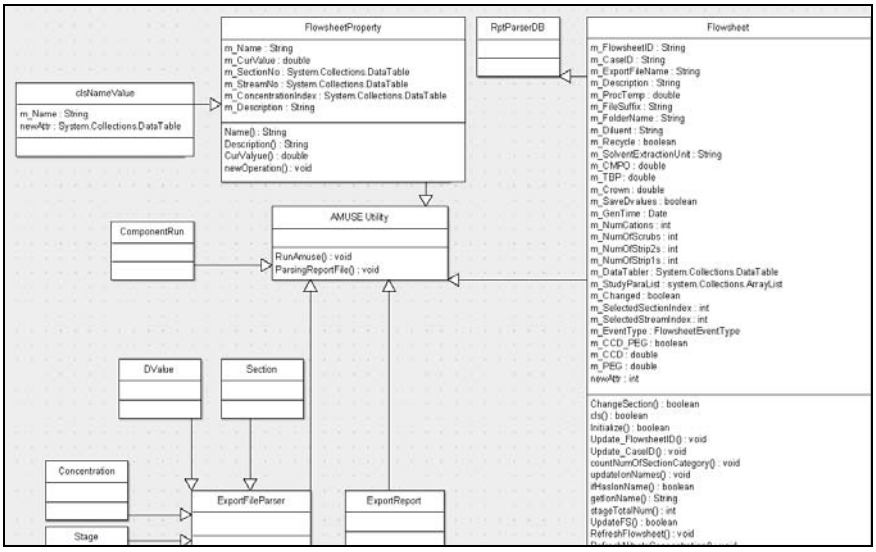

Figure 13. Class diagram for the AMUSE middleware interface.

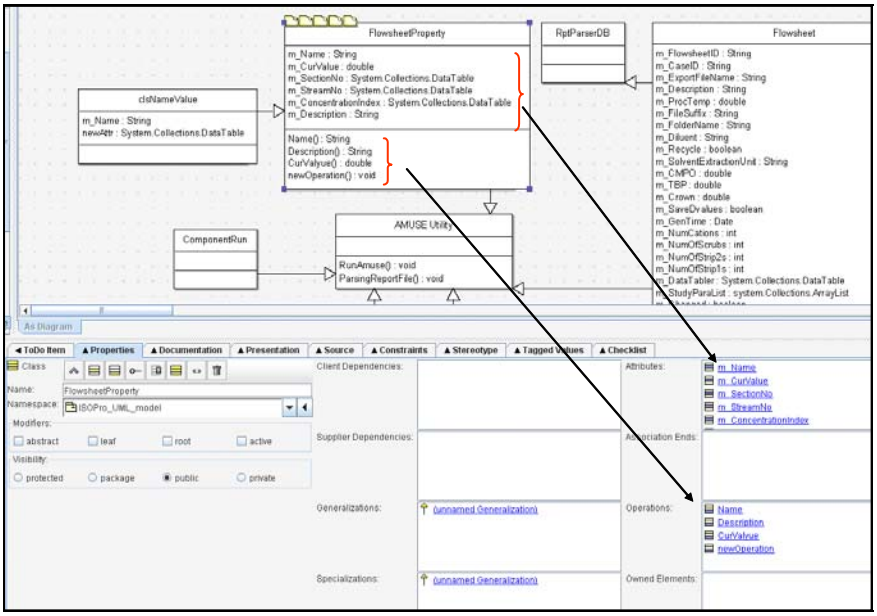

Figure 14. Detailed design factors for the "Flowsheet" module is better documented in the property sheet shown in the bottom.

Electrochemical Separation of Curium and Americium (Task 25).

This task successfully prepared alkylamine and immidazolium RTIL solutions and measured the potential windows previously. The preliminary electrochemical characterization of Eu in RTIL ($[MeBu_3N][NTf_2]$) was successful and showed that RTIL solutions could be used to electrodeposit the metal species. The results demonstrate the advantage of performing

voltammetry in RTIL solutions. These studies have been extended to include UO_2, UO_3, and Uranyl Carbonate in RTIL solutions. The goal of these measurements is to identify the electrochemical characteristics of the species in the RTIL and evaluate the feasibility of tailored electrodeposition of Uranium species. $UO_2(OH)_2$ and $UO_2(N(Tf)_2)_2$ have been examined with decent resolution of the Uranium redox chemistry. These are preliminary studies that will continue to examine the species in RTIL solutions. The solubility using FTIR (Figure 15) was examined to ensure the complexation of the U species with the TFSI anion to enhance the solubility.

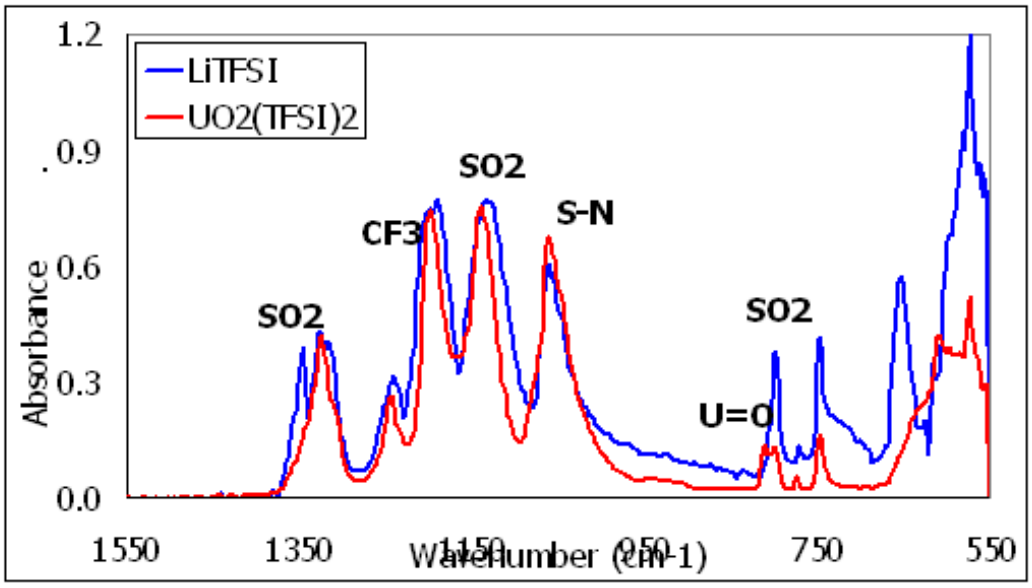

Figure 15. FTIR of LiTFSI salt (blue) and UO_2TFSI_2 complex.

The data clearly shows the loss of band associated with the complexation of UO_2 and the ligand with the emergence of U=O bands at 900 cm^{-1} and the loss of bands at 1200 and 1370 cm^{-1}, respectively. The voltammery associated with this species is quite complex (Figure 16).

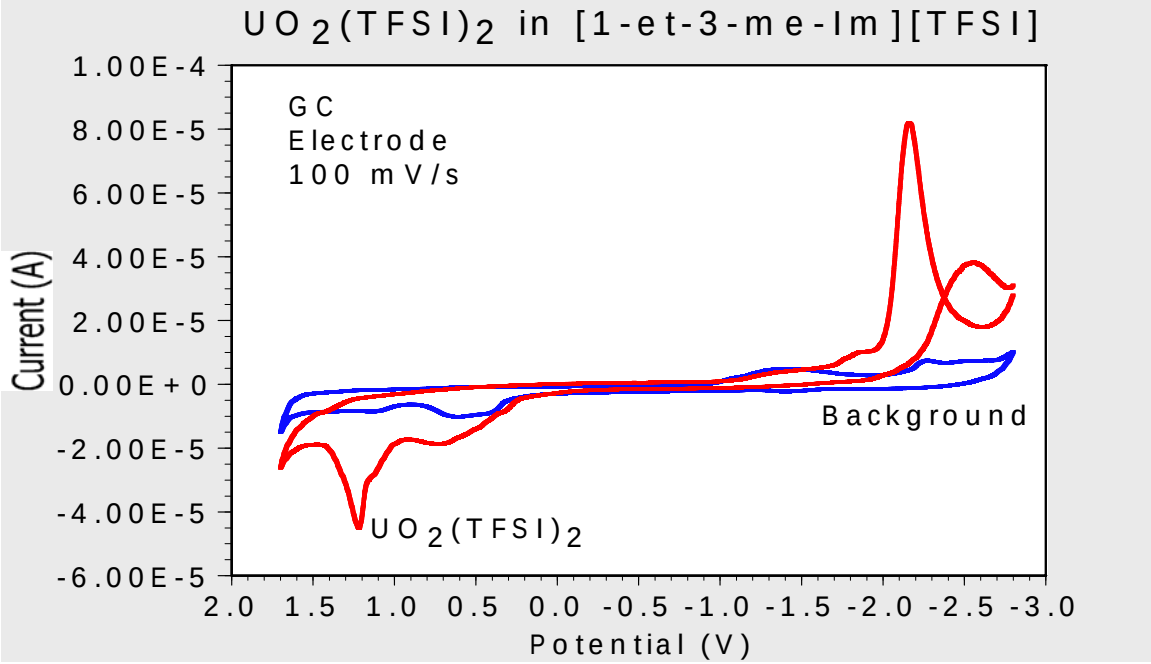

Figure 16. Electrochemistry of UO2(TFSI)2 in 1Et3MeIm(TFSI) RTIL.

Finally, the solubility of $UO_2(CO_3)$ in $Me_3NnBu(TFSI)$ bubbled with Argon to remove decompose carbonate and form UO3 directly in the RTIL was examined (Figure 17). The results are promising (and show) multiple redox processes. It is hoped that U can be electrodeposited from these solutions.

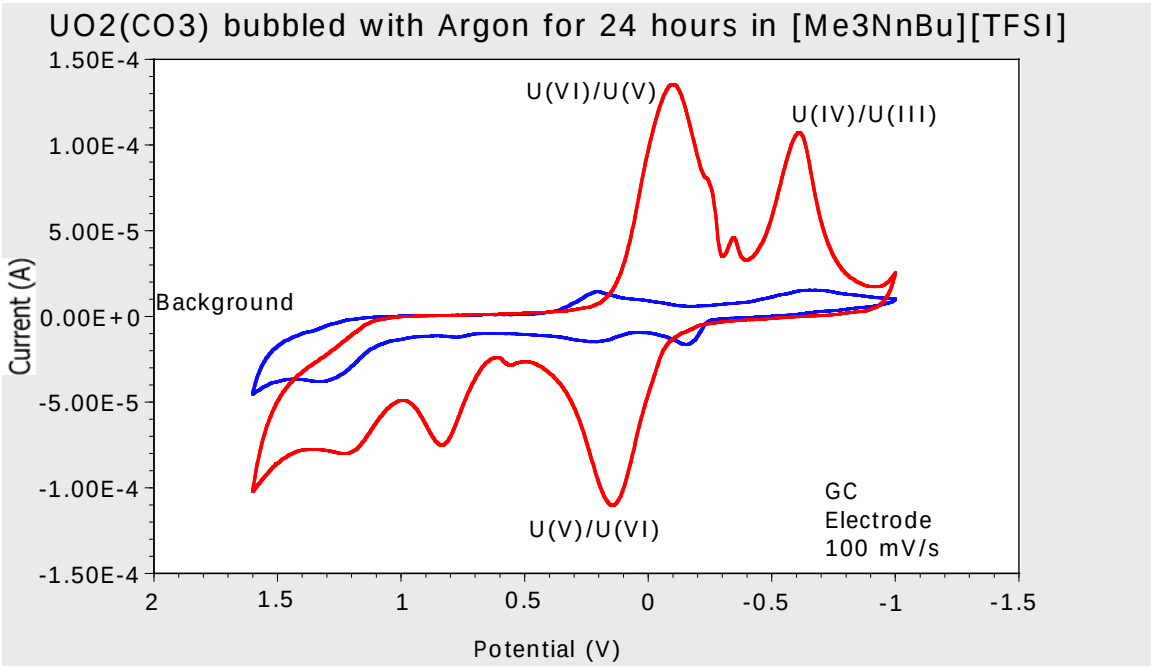

Figure 17. Electrochemistry of UO_3 in RTIL.

Fundamental Chemistry of U and Pu in the TBP-Dodecane-Nitric Acid System (Task 26).

Investigation of Optical Spectroscopy Techniques for On-Line Materials Accountability in the Solvent Extraction Process (Task 29).

Application of UV-Visible Spectroscopy for Determination of Uranium Concentrations

Experiments to evaluate the chemical concentration and speciation of uranium in the organic phase of the UREX and PUREX process continued. To confirm the calibration curves in the organic phase for the UV-Visible absorbance technique, two confirmatory methods for the determination of uranium in the organic stream were used: liquid scintillation counting of the organic stream and ICP-AES measurements of the pre- and post- equilibrated aqueous phase to determine the concentration of the extracted uranium. Using these methods, the calibration solutions for the optical spectroscopy systems were verified, allowing the direct calibration of the UV-Visible spectrometer for uranyl in the organic stream.

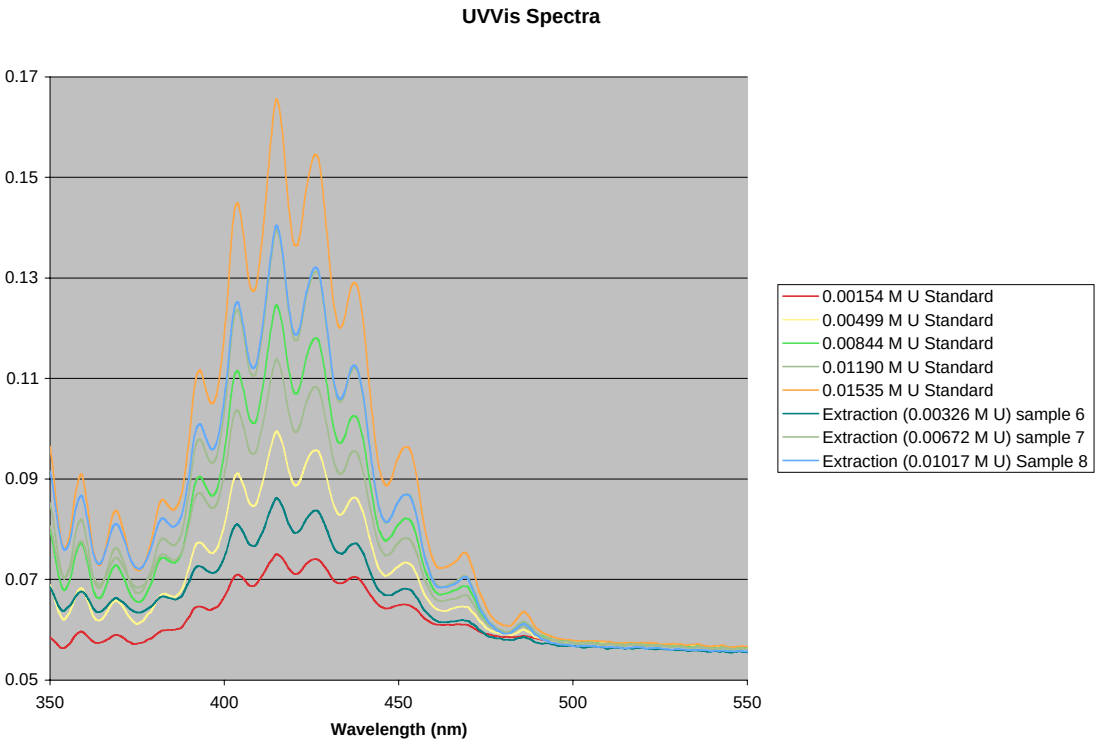

Figure 18. UV-Visible Absorbance Spectra for $U(^{6+})$ in the Organic Phase.

Initial investigations of the organic system have focused on determining detection limits and range of linearity for the organic phase in equilibrium with a 1 M nitric acid aqueous phase. Experiments are continuing to examine the impact of nitrate, acid, and AHA on the detection limits and speciation in the organic phase. In parallel to these experiments to determine the detection ranges in the organic stream, research into the chemical speciation in the organic phase continues. To support this phase of the work, methods were developed to determine the nitrate

concentration in the organic phase by ion chromatography (IC), as well as the acid concentration by potentiometric titration.

Effects of Iron and fission products on Uranium Response with Laser Fluorescence and Visible Spectroscopy in the Aqueous System

Studies were continued into the effect of iron (III) on the luminescence behavior of uranium. The initial studies examining feed stream nitrate and acid conditions were extended to lower acid and nitrate concentrations to support the efforts to understand the fundamental interaction mechanisms as well as to bind the impact in other process streams. Through these experiments, it was noted that the quenching behavior was affected by the acid concentration, with the quenching being suppressed at higher acid [H^+] concentrations. The potential to exploit this effect for analyzing samples under feed stream conditions by the titration with concentrated acid is currently being analyzed.

In addition to Fe, which is primarily a degradation product, there is concern about the transition metal fission product contribution to both the luminescence and absorption spectra. The available literature is thin concerning the effects of these ions in the systems of interest. However, several papers note that the quenching effect of these transition metals are similar to those of Fe. The molar absorptivities and related UV-Vis spectrums of the fully oxidized species is also lacking in the literature. Pursuant to this, a matrix of 17 potential FP interferants has been compiled. The impact of these potential interfering elements on the laser fluorescence and absorbance spectroscopy of uranium will be examined over the next quarter. The goal is to evaluate the basic behavior of each of these metals and determine whether any significant quenching, co-fluorescence, or co-absorbance exists which will interfere with the determination of uranyl concentrations in the UREX process.

Combined Radiation Detection Methods for Assay of Higher Actinides in Separation Processes (Task 30).

Purpose and Problem Statement

Monitoring of higher actinides (HA--includes neptunium, plutonium, americium, and curium) during the separation of used nuclear fuel has been identified as a critical research area for GNEP. Recycling of used fuel by chemically separating it into uranium, fission products, and HA would be the first step in this new fuel cycle. Material Protection, Accounting, and Control (MPAC) is necessary for materials accounting, criticality monitoring, and assurance of proliferation resistance. The objective of this MPAC project is to develop and/or evaluate technology to detect and accurately measure quantities of HA in used fuel assemblies and processing systems, without taking frequent samples. Process systems may include separations batches, pipelines, storage tanks, and fuel fabrication equipment. A variety of measurements may be combined to calculate flow rates of actinide elements with a to-be-determined precision.

In the MPAC project, faculty and students are investigating the potential to use combined neutron and other detection systems to measure quantities and isotopic constituents of HA during separations and intermediate storage. This will require knowledge of the nuclear and decay

characteristics of materials during processing, the development of conceptual designs of monitoring systems, radiation transport studies to develop an understanding of operational regimes, and experiments to confirm performance. In addition, both passive and active concepts will be investigated, including collaborations with the Idaho Accelerator Center (IAC) at Idaho State University (ISU) to use electron linacs for producing photoneutrons in situ, for photon activation of HA, or for stimulating emissions processes (e.g. x-ray fluorescence).

Summary Report for July to September 2007

During the first two months of this period little progress was made; graduate research assistants were working in summer internships with Bechtel-SAIC Corp. at the Yucca Mountain Project. Their work with BSC gave them additional experience in reactor physics modeling and analysis. They returned to UNLV at the end of August and resumed studies and research.

GRA Quentin Newell collaborated with Los Alamos to complete a benchmark exercise modeling the LANL Lead Slowing Down Spectrometer (SDS). The energy of neutrons measured in a neutron detector with an SDS can be characterized by the equation $E = K/(t+t_0)^2$, where K and t_0 are characteristic energy-time correlation constants. These values were calculated with the LANL MCNPX code and were successfully benchmarked against the LANL model, producing results within Monte Carlo statistical uncertainty limits.

During the interim, collaboration with the V. G. Khlopin Radium Institute was developed for an upgrade to and maintenance on the Neutron Multiplicity Detector System (NMDS). A work package was developed and submitted to DOE/NE and a UNLV-KRI contract was completed. KRI began design studies and developed a plan for adding a multi-plate plastic scintillator anti-coincidence system to reduce background and provide greater neutron-muon discrimination. KRI submitted two progress reports and initiated procurement of components for the upgrade, which will be installed in November.

In preparation for the KRI visit, GRAs Timothy Beller and Ryan LeCounte (TRP Task 35) re-connected the NMDS to the original Russian data acquisition system and several neutron multiplicity counts were conducted to confirm its performance. The data files were transmitted to KRI where they were evaluated. All detectors appear to be operating as they were when the system was initially delivered and set up at UNLV several years ago.

Synthesis and Properties of Metallic Tc and Tc-Zr Alloys as a Radioactive Storage Waste Form to Stabilize the Tc Waste Stream of the UREX+1 Process (Task 33).

Evaluation of Cs/Sr Waste Form for Long Term Storage and Disposal (Task 36).

Waste Form/Container Material Compatibility Testing

Heats of hot-rolled A36 carbon steel, 304L stainless steel, and 316L stainless steel were received from PDM Steel Services. Sample coupons (3.5” by 2.5”) were cut from the as received plates

for the compatibility testing in the on-campus machine shop. For the corrosion experiments, it is essential that the surface of the metal samples be clean, uniform, and well characterized. Initial attempts to polish the surface of the coupons on campus using the CNC mill in the campus machine shop were not able to produce a uniform surface (Figure 19). Off-campus machine shops capable of polishing the samples to the required smoothness have been identified, and the samples will be sent off for machining in the next quarter.

In parallel with the sample preparation work, the characterization work for the as received materials has begun. X-ray diffraction powder patterns for the steels confirm that the materials are the correct composition and consist of a single composition. Optical microscopy of the steel samples will be performed over the next quarter by students in the graduate physical metallurgy class (MEG 702).

Waste Form Synthesis and Characterization

Samples of the Volclay^{TM} bentonite waste former material were obtained from American Colloid in two 2 kg batches, one from the HPM-20 product line, and the other from the 325 mesh product line. While neither batch is an exact match for the lot being tested by the Argonne National Laboratory team (Volclay^{TM} HPM-20, 425 mesh), both are from the same source location and should be very similar in composition and particle size. The as received material was characterized using a number of techniques. The water content of the material was determined by loss-on-ignition at 150 °C and 950 °C (sequentially). The primary elemental composition of the clay material was determined by dissolving the clay into a glass flux and analyzing the resulting fusion by x-ray fluorescence. Trace elemental composition was determined by x-ray fluorescence using the dried clay material compressed in a wax matrix. Using powder x-ray diffraction to examine the mineralogy of the samples, the bentonite clay material was found to contain quartz, Beidellite, and Montmorillonite. Quantitative phase composition will be determined by Reitveld analysis (underway). The surface area of the oven-dried (150 °C) bentonite clay was determined by the Brunauer-Emmett-Teller (BET) method to be 11.07 m^2/g for the HPM-20 material, and 13.38 m^2/g for the Volclay^{TM} 325 mesh material.

Table 1. Major Element Composition of Bentonite Waste Former.

	Volclay™ HPM-20	Volclay™ #325
Loss on Ignition (150 °C)	6.89%	6.41%
Loss on Ignition (950 °C)	6.03%	7.53%
Loss on Ignition (Total)	12.92%	13.94%
Major Element Composition (based on Oxide Mass)		
SiO_2	58.2%	55.2%
Al_2O_3	18.9%	18.0%
TiO2	0.14%	0.15%
CaO	1.45%	3.34%
MgO	2.53%	2.68%
Na_2O	1.69%	1.84%
Fe_2O_3	3.46%	3.84%
K_2O	0.44%	0.59%
P_2O_5	0.05%	0.06%
MnO	0.01%	0.02%
S	0.18%	0.28%
Total (including H2O)	99.95%	99.9%

Table 2. Trace Element Composition of Bentonite Waste Former.

Compound	Volclay™ HPM-20	Volclay™ #325
Sc	9.30 ppm	7.22 ppm
V	0.84 ppm	1.96 ppm
Ni	6.36 ppm	8.14 ppm
Cu	6.16 ppm	5.94 ppm
Ga	31.24 ppm	29.64 ppm
Rb	15.77 ppm	19.87 ppm
Sr	309.00 ppm	279.74 ppm
Y	45.37 ppm	48.58 ppm
Zr	173.18 ppm	195.08 ppm
Nb	34.13 ppm	28.94 ppm
Mo	3.04 ppm	3.41 ppm
Ba	335.96 ppm	321.83 ppm
La	51.49 ppm	39.82 ppm
Hf	6.27 ppm	6.00 ppm
Pb	35.58 ppm	46.02 ppm
Th	47.15 ppm	45.52 ppm
U	15.61 ppm	14.65 ppm

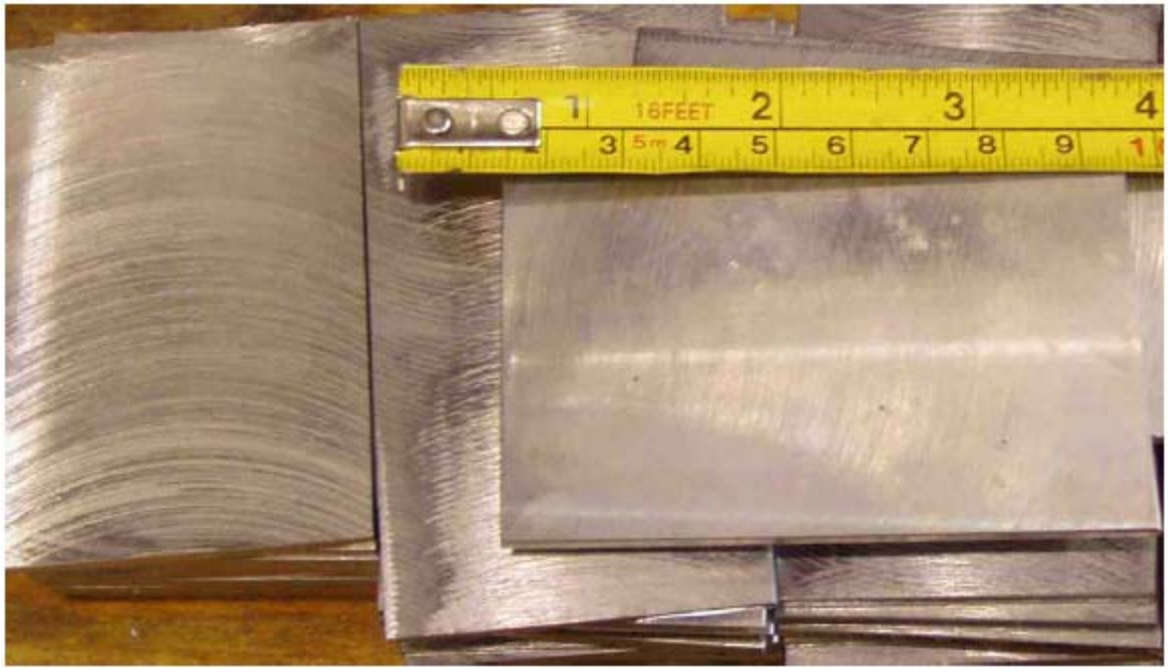

Figure 19. CNC milled surfaces for test sample coupons.

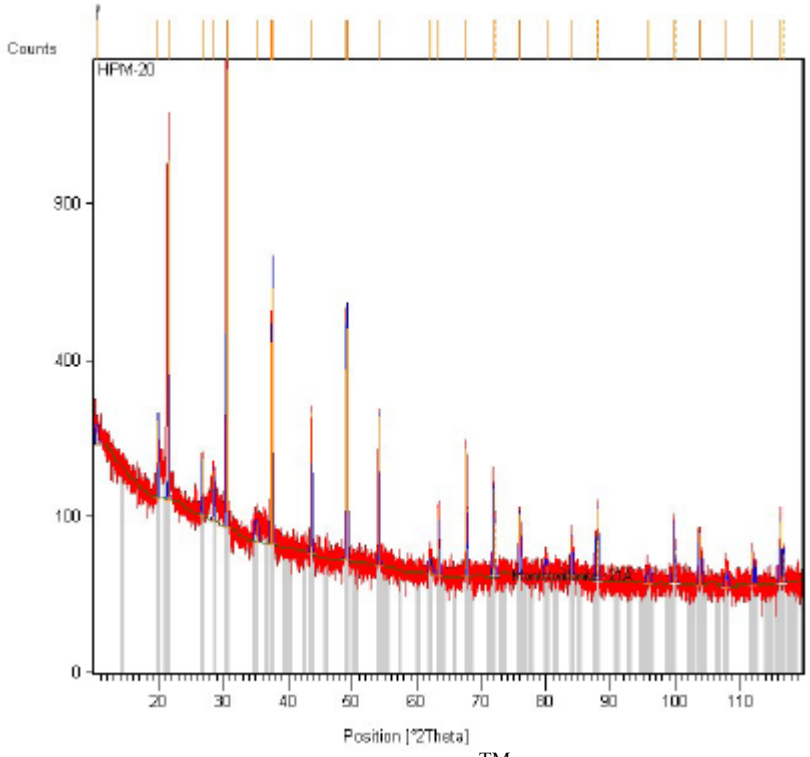

Figure 20. Powder XRD Pattern for Volclay™ HPM-20 (with LaB_6 standard).

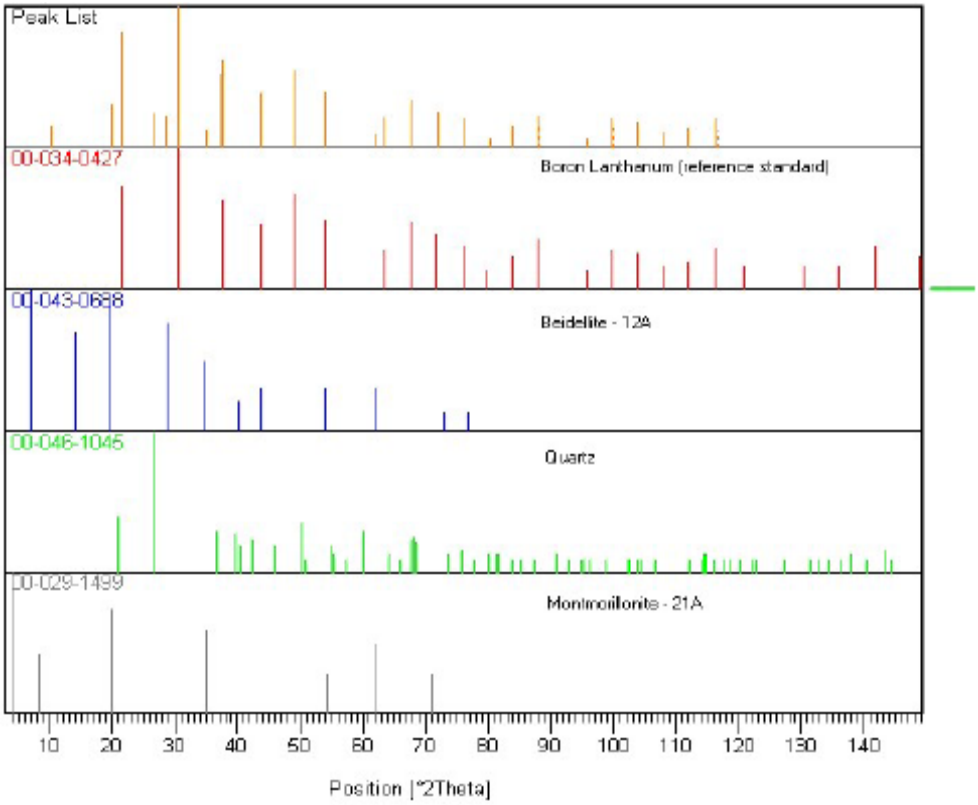

Figure 21. Powder XRD Stick Pattern for Volclay^{TM} HPM-20 (with LaB_6 standard).

TRANSMUTATION SCIENCES

Corrosion Mechanisms and Kinetics of Steels in Lead-Bismuth Eutectic (Task 18)

Impact of Silicon on Corrosion Resistance of Stainless Steels in LBE Systems (Task 20).

Debajyoti Maitra, one of the Ph.D. students, successfully defended his doctoral dissertation July 2007. The detailed research findings based on his overall work are contained in his dissertation titled "Tensile deformation and environmental degradation of T91 grade steels with different Si content". A majority of his work has already been presented in previous quarterly reports, with an exception of his stress corrosion cracking (SCC) testing results, performed in an acidic solution under controlled cathodic and anodic electrochemical potentials. With respect to elevated temperature tensile testing of T91 grade steels, the tensile data of these alloys containing four levels of silicon (Si) content were also presented earlier.

The results of tensile testing performed at a strain rate of $5x10^{-4}$ sec^{-1} have exhibited an interesting metallurgical phenomenon, known as dynamic strain ageing (DSA). Since, the occurrence of DSA is influenced by both temperature and strain-rate, additional tensile testing has recently been performed at three temperatures (200, 300 and 400ºC) under three strain-rate conditions (10^{-2}, 10^{-3} and 10^{-4} sec^{-1}). It is anticipated that the magnitudes of the resultant activation energy (Q) and work-hardening index (n) determined from recent studies will enable

the development of a plausible deformation mechanism of T91 grade steels as a function of Si content. Simultaneously, significant efforts have been made to evaluate impact energy of T91 grade steels as functions of both temperature and Si content that led to the establishment of ductile-brittle-transition-temperatures (DBTT) based on the measured impact energy of these alloys.

The tensile properties of 12Cr-1Mo steels containing 3 and 4 weight percent (wt%) Si have also been determined at temperatures up to 550ºC. As to the corrosion behavior of these alloys, efforts were also made to determine their localized corrosion susceptibility using an electrochemical polarization technique. The susceptibility of these alloys to SCC has also been evaluated using the slow-strain-rate (SSR) technique, with and without applied electrochemical potentials. The magnitudes of the applied potentials were based on the corrosion potential (E_{corr}) determined from the localized corrosion studies. The key results obtained in the most-recent quarter are summarized in the Highlights section.

Ongoing/Future Work

- Performance of plain strain fracture toughness (K_{IC}) testing of T91 grade steels using compact tension specimens at ambient and elevated temperatures.
- Performance of SCC testing using pre-cracked and wedge-loaded double-cantilever-beam specimens of both T91 and 12Cr-1Mo steels.
- Inclusion and analyses of recent experimental data in dissertation/thesis to be defended during fall 2007.

Tables & Figures

Table 3. Tensile Parameters versus Strain-Rate and Temperature.

Temperature/ Strain rate (sec^{-1})	**Si Content (wt.%)**	**200ºC**			**300ºC**			**400ºC**		
		YS (ksi)	**UTS (ksi)**	**Failure Strain (%)**	**YS (ksi)**	**UTS (ksi)**	**Failure Strain (%)**	**YS (ksi)**	**UTS (ksi)**	**Failure Strain (%)**
10^{-2}	0.5	116	131	19.34	110	127	17.4	107	118	18
10^{-3}		116	131	20.17	111	127	18.4	114	128	19.1
10^{-4}		117	133	20.55	115	129	19.5	111	121	20.6
10^{-2}	1.0	119	134	19.9	111.4	128.8	19	107.3	123.4	20
10^{-3}		118	134	20.7	114	131.6	19.5	106.8	124.6	19.8
10^{-4}		116	135	21.2	113.4	132.3	20.7	107.5	125.0	22.8
10^{-2}	1.5	114	132	21.5	110	128	19	108	125	20
10^{-3}		115	132	21.9	110	130	21	107	126	21.3
10^{-4}		114	133	22.7	108	132	21.5	97	119	26

10^{-2}	2.0	109	131	20.5	103.4	126.1	18.5	93.6	120.5	19
10^{-3}		106	130	22.9	103.9	128.7	21.8	96.2	119.4	23.7
10^{-4}		105	132	24.9	106.9	133.4	23.1	97.9	121.6	24.5

Table 4. Results of Charpy Testing.

Heat No.	**Temperature (ºC)**							**DBTT (ºC)**
	-40	**25**	**75**	**125**	**230**	**340**	**440**	
2403	15	19	27	48	59	62	63	90
2404	8.5	13	18	38	47.5	49	49	95
2405	4.5	8	12.5	19	31	38	39	140
2406	3	6	8	13	23	28	30.5	150

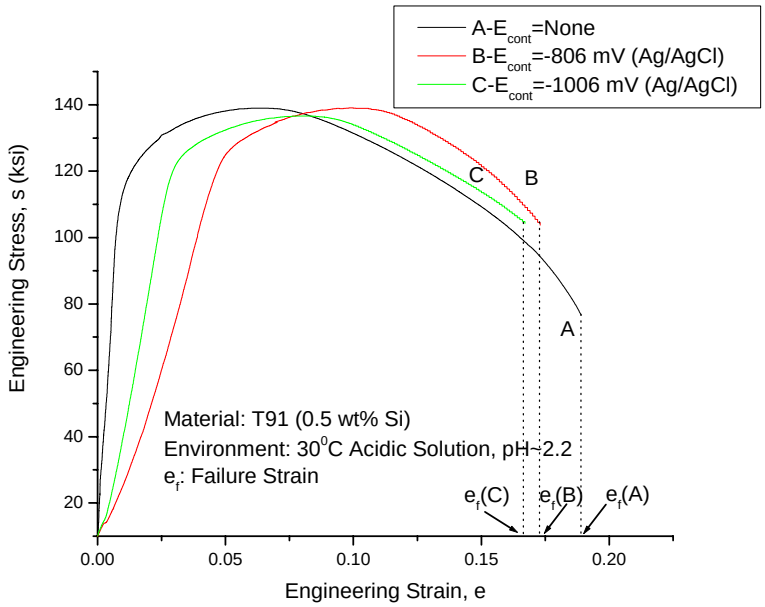

Figure 22. s-e Diagrams vs. Cathodic E_{cont}.

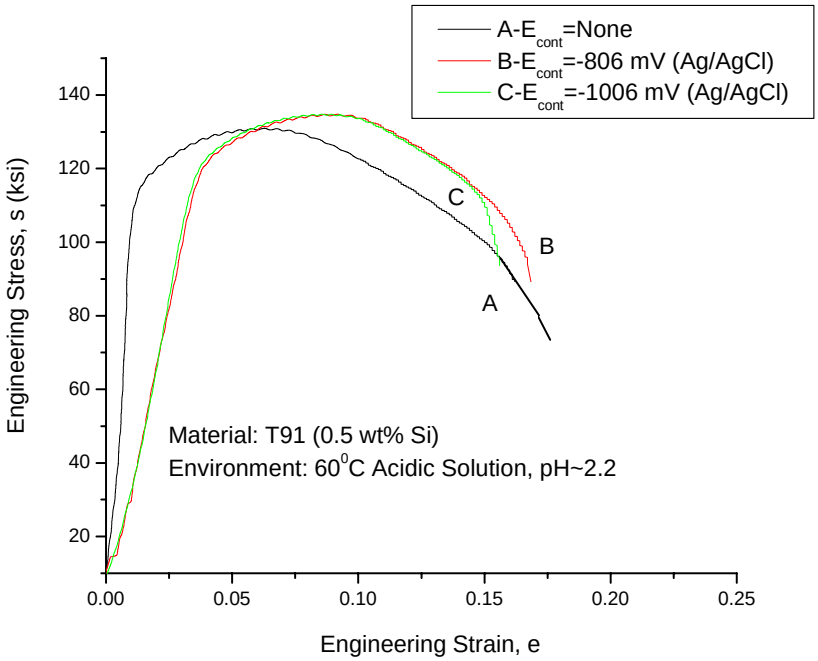

Figure 23. s-e Diagrams vs. Cathodic E_{cont}.

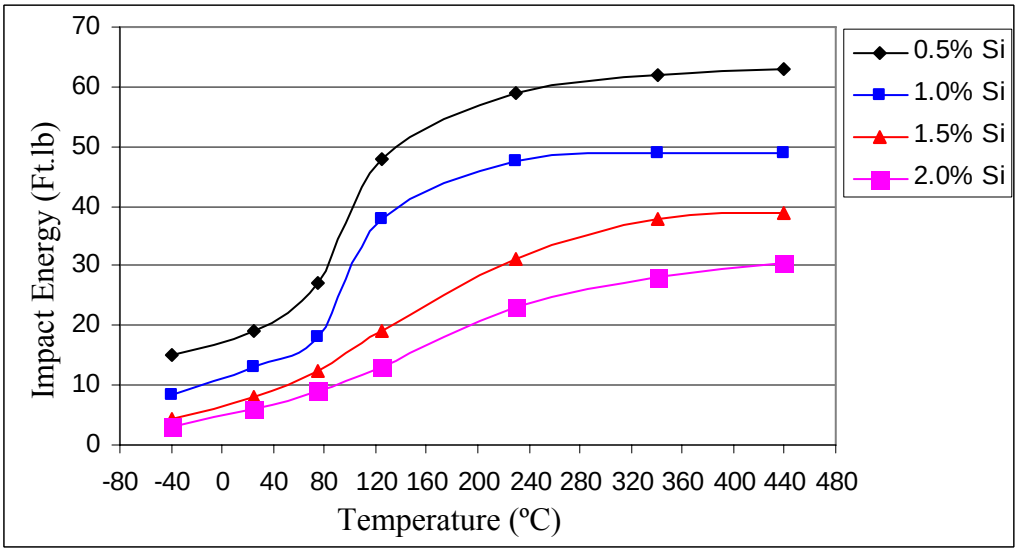

Figure 24. Impact Energy vs. Temperature.

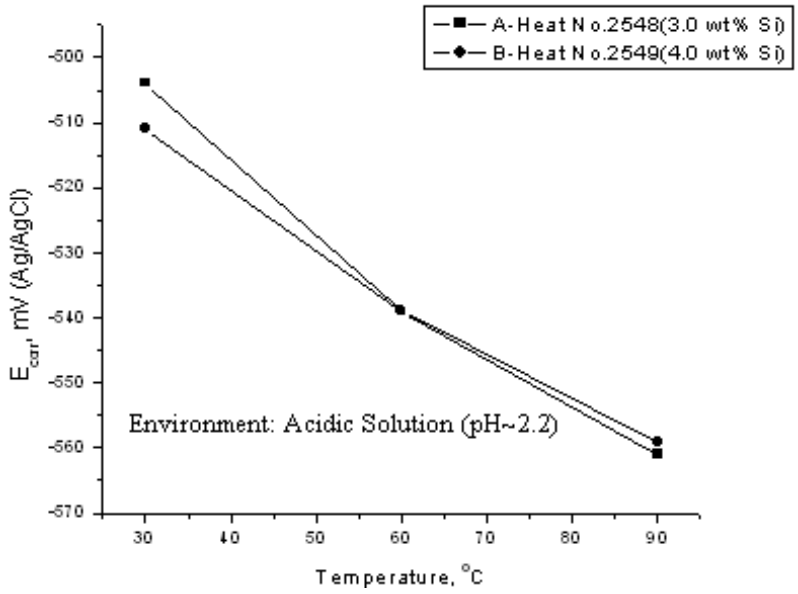

Figure 25. E_{corr} vs. Temperature for 12Cr-1Mo steels.

Oxide Film Growth Modeling in LBE Systems (Task 21).

Specimens of US martensitic steel, Batman 28, were tested in flowing LBE loop at a temperature of 743 K. The flow velocity was set at 1.9 ± 0.1 m/s, and the oxygen concentration was maintained at (1-2) x 10^{-6} wt%. The total oxidation layer thickness was measured to be 12.0 μm, 15.0 μm, and 17.0 μm after 1,000, 2,000, and 3,000 hours of exposure, respectively. The inner layer thicknesses are estimated to be 10.0 μm, 2.0 μm, 12.5 μm and outer layer thicknesses to be 2.5 μm, 14.0 μm, 3.0 μm for 1,000, 2,000, and 3,000 hours, respectively. The scale removal rate in such an environment can be estimated by K_r = 7.0 x 10^{-13} m/s. The thickness growth of the duplex oxide layer has been numerically calculated from the present model and has been compared with the experimental data. The numerical results from the present model agree with the experimental data (Figure 26). The thicknesses of the total oxide thickness, the inner oxide thickness increase with time following a parabolic law. Obviously, the estimation of oxide growth from the present model agrees with the Wagner's theory. The thickness of the outer oxide layer increases fast at the initial stage and the growth speed slows down after the initial stage. One of the reasons for this phenomenon is the scale removal effect. Another reason is the oxygen diffusion speed slows down when the oxygen concentration gradients in oxide and steel become smaller after oxygen diffused into the oxide and steel. From the benchmark, the scale removal effect is an important influence to the oxidation process. The diffusion-controlling oxidation model shows the ability to estimate the oxide growth in high temperature metal flow which contains oxygen.

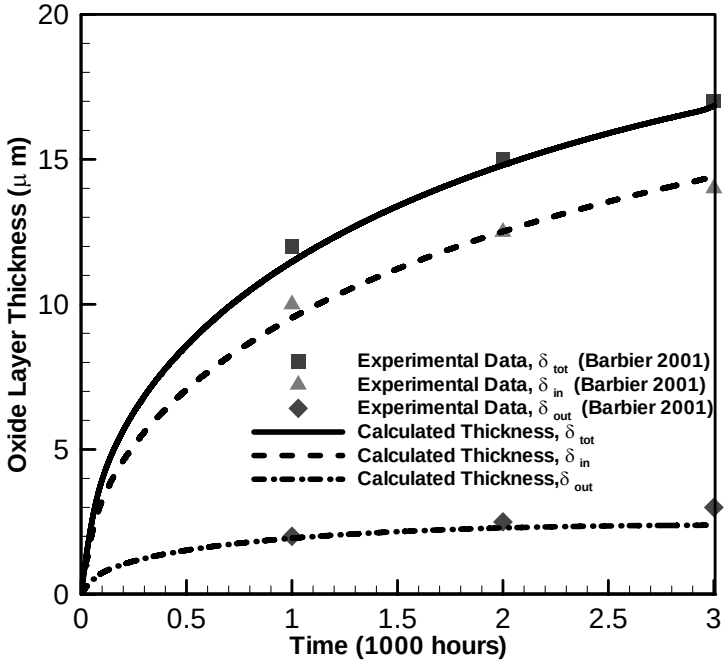

Figure 26. Benchmark with the experimental data of stainless steel in flowing LBE.

Corrosion Barrier Development for LBE Corrosion Resistance (Task 23).

Reactor Physics Studies for the AFCI RACE Project (Reactor-Accelerator Coupling Experiments Project (Task 27).

Decoupling and Disturbance Rejection Control for Target Circulation (Task 31).

After testing the new algorithm for the TC-1 thermal and alarm systems in last quarter, the TC-1 can be operated at static status with a working temperature of 200 °C without a pump operation. During this quarter, some modifications of the TC-1 loop were made to reduce the extra heat generated by the Electromagnetic pump, which is beyond the requirement of this Task.

The installation of variable frequency drive, which is used to change the frequency of input power to the EM pump (Figure 27a), was accomplished first. The optimized input frequency will enhance the efficiency of EM pump, which leads to less heat being released from it.

Second, the additional cooling system was built up to get rid of heat from the well thermal isolated TC-1 container (Figure 27b). One cooling media is the compressed air passing through the high temperature heat exchanger in the TC-1. The other cooling media is water passing through the radiation shielding block, which does not directly connected to the TC-1 primary loop and has surface temperature lower than 100 °C.

(a)

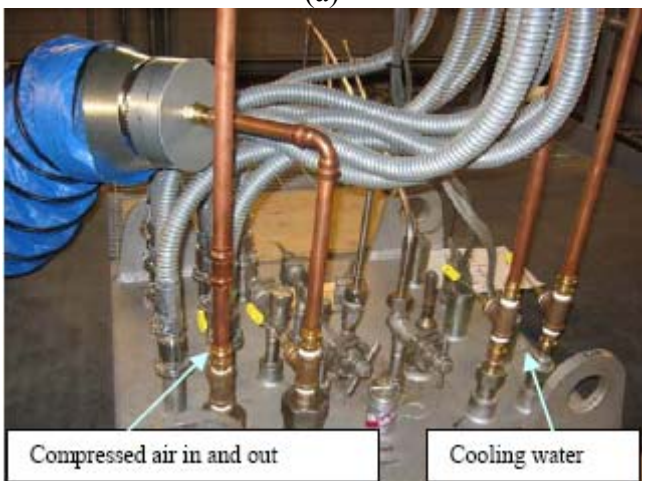

(b)

Figure 27. (a) Variable frequency driver from Siemens and (b) Cooling system with compressed air and water on the top of TC-1.

Magnetohydrodynamic Simulation of Electromagnetic Pump in TC-1 (Task 32).

Objectives and Scopes

A fundamental understanding of the combined hydraulic, thermal, and electromagnetic phenomena occurring in electromagnetic induction pumps is essential for their safe use in neutron accelerator targets for nuclear waste transmutation and in Gen IV nuclear reactors. The goal of this task is therefore to develop the expertise with EM pump technology that will allow researchers at UNLV to aid in the design, fabrication and safe operation of EM pumps for nuclear applications.

Online Database Activity

An on-line literature database has previously been set up at:

http://nstg.nevada.edu/mmrg/research/LitSurvey/EMP-Literature.html

This literature database contains over 120 entries. One of the issues that arose during development was that only a single user had access to enter new articles into the database. This meant that quite often, valuable articles were not being made available to all users. It was decided to develop a wiki-based database to allow all members of the research group to enter and edit database entries. According to Wikipedia (the most well-know wiki), a wiki is "a collaborative website which can be directly edited by anyone with access to it". One of the advantages of wikis is that they allow easy exchange of information between individuals working on a single project. It was initially planned for the wiki to be fully functional by the end of August, 2007. However, the beta-testing stage, in which various wiki applications were evaluated for use in the project, was longer than expected. At this point in time, the dokuwiki package has been selected for use, is currently installed on one of the College of Engineering servers, and the articles in the database have been transferred to the new server.

MHD Solver Development

The results from a numerical model of the TC-1 loop were presented at both the ASME IMECE 2006 conference and the Comsol Users Conference 2006. The model presented at these conferences calculated only the EM phenomena (current density, magnetic field, and electromagnetic body forces) in the pump. The velocity of the liquid in the pump was specified, not calculated.

The next generation of the model was to have used code developed in-house at UNLV as the core of a fully-coupled MHD solver. Issues with this software development have made it more attractive to use the commercial code Fluent for the CFD calculations in the solver. The initial fluid flow calculations have been completed using Fluent and the undergrad working on the project is working on integrating the EM body forces into the Fluent model.

Criticality Studies for UREX Processes (Task 35).

Purpose and Problem Statement

The completion of criticality experiments for mixtures of higher actinides (HA, includes neptunium, plutonium, americium, and curium) that will be created during the separation of used nuclear fuel may be required prior to construction of prototype plants such as the Engineering-Scale Demonstration (ESD) and the Advanced Fuel Cycle Facility (AFCF) for the Global Nuclear Energy Partnership (GNEP). Proposed mixtures and concentrations of HA covering a wide range of conditions must be examined theoretically and experimentally to demonstrate criticality safety in advance of construction of a processing facility. Theoretical studies may be limited because of insufficient nuclear data for the rarer isotopes of plutonium (Pu), americium (Am), curium (Cm), and neptunium (Np). These data limitations include reaction cross sections in some energy regimes, thermal feedback coefficients, and delayed neutron fractions (β).

This project will conduct criticality sensitivity studies to support the development of future fuel cycle facilities. The first step in determining requirements for criticality studies is an examination of past experiments and studies as well as available data bases. Further sensitivity studies will determine what kinds of experiments should be performed to insure criticality safety in advanced processes. This information can then be used to formulate an optimum set of experiments that can be analyzed in advance using state of the art radiation transport codes. As these facilities and experiments will include complex geometries, MCNP will be used in these sensitivity, scoping and design studies. The work may also require generation of new cross section libraries and thermal scattering ($S(\alpha,\beta)$) coefficient data bases. Future criticality studies may include cross section sensitivity studies and design of critical experiments including dilute mixtures of Pu, mixed higher actinides in solution, and fuels.

Summary Report July to September 2007:

During the first two months of this period little progress was made because the graduate research assistants were working in summer internships. Lakeotes is working with National Security Technologies, LLC (NSTec) at the Remote Sensing Laboratory of the Nevada Test Site. LeCounte was in a summer internship with Bechtel-SAIC Corp. at the Yucca Mountain Project. They returned to UNLV at the end of August and resumed their studies and research.

The project scope continued to be defined, and the appropriate focus on cross-section sensitivity studies versus design of required criticality experiments continued to be examined. Students continued to collect information on code systems and references on criticality and sensitivity studies and to research cross section uncertainties for Am and Cm at room temperature in UREX+1 separations processes. Previously, MCPX, MCNPX, SCALE, and data libraries for processing cross sections and conducting sensitivity studies were acquired and installed. In this quarter, NJOY 99 was acquired and installed for processing cross sections for sensitivity studies. In addition, sample problems for Scale 5.1 were completed to ensure accuracy of the code. However, an issue with the FORTRAN compiler has prevented the processing of cross sections. Work with the authors of the code system at LANL is being conducted to solve the problem.

Deep Burn Separations and Repository Behavior.

Spectral measurement of UV absorbance of Triton X-114 and 8-Hydroxyquinoline

In preparation for sequential extractions in the cloud point extraction system, a method for measuring the organic content of the light phase so that in sequential extractions, the same extraction system can be present. Spectra were taken of triton X-114 and 8-hydroxyquinoline to assess the feasibility of measuring the organic content of the aqueous (light phase) after each extraction.

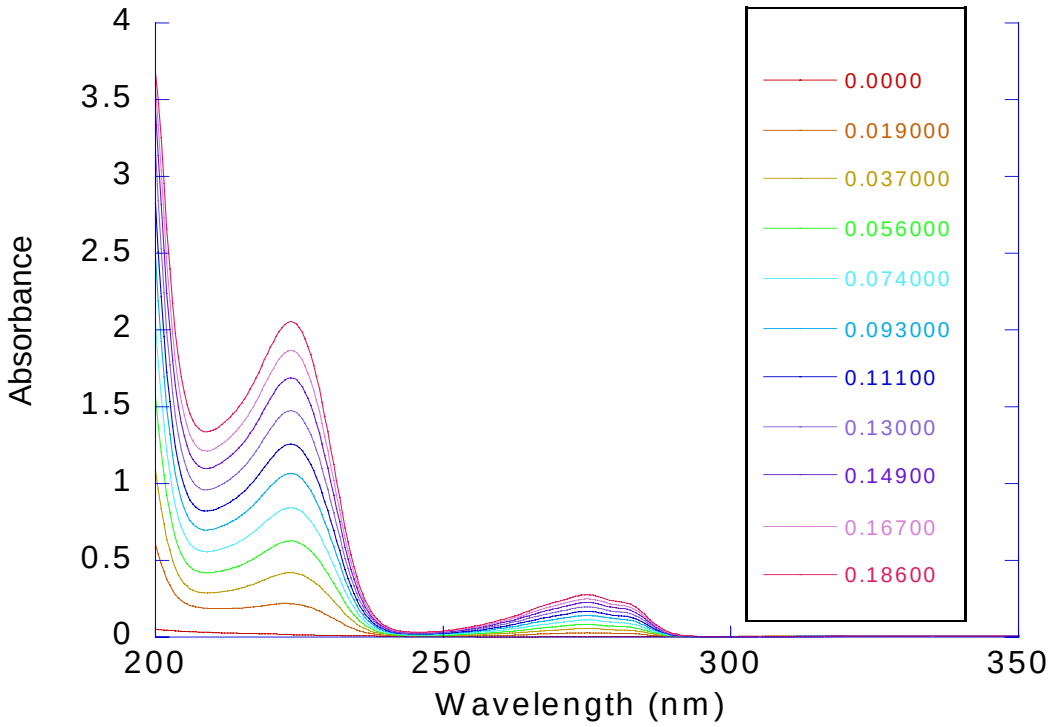

Figure 28. UV absorption spectra for Triton X-114. Plot series labels show the molarity of Triton X-114 in mM.

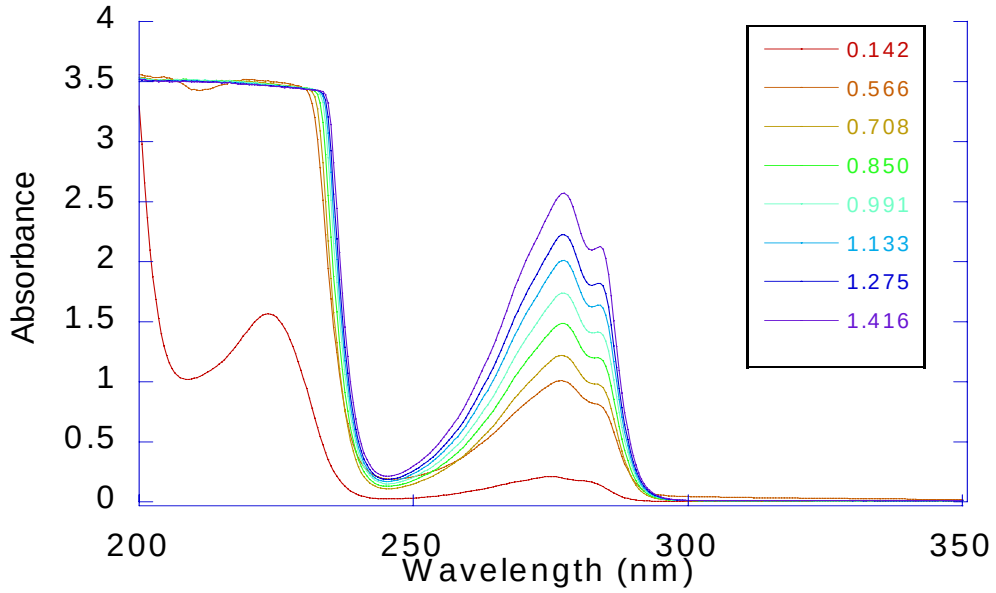

Figure 29. Absorptivity of Triton X-114 for peak at 277 nm. Series labels represent the Triton X-114 molarity in mM.

There was some difficulty measuring the 2 samples at concentrations of 0.283 and 0.425 mM. At room temperature these solutions began forming micelles due to the cloud point phenomenon, and when the solutions were refrigerated condensation, or some other optical interference,

caused the data to become suspect. The data was discarded and will be measured at a future date if it is deemed necessary. From the spectra taken a molar absorptivity of the following was obtained:

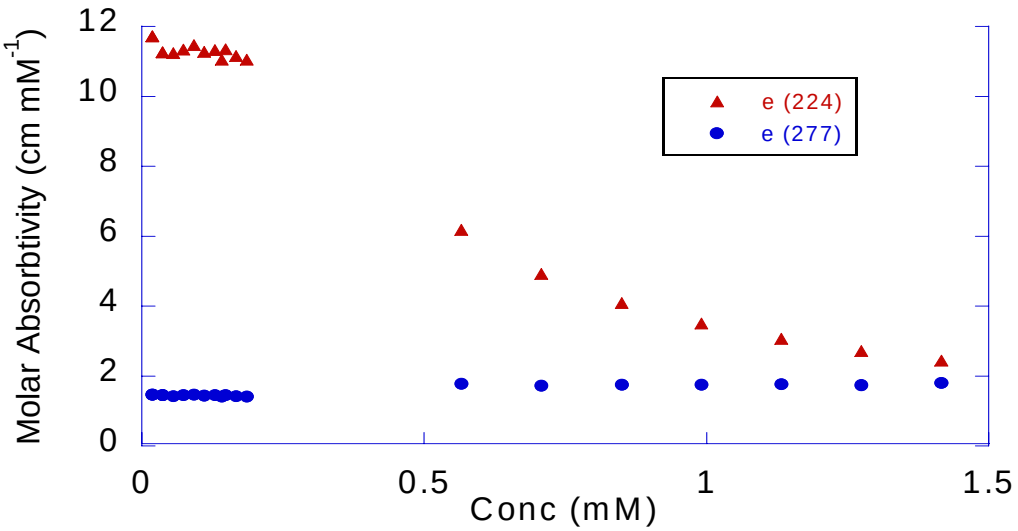

Figure 30. Evaluated molar absorptivity of Triton X-114.

The molar absorptivity for triton X-114 appears to be best used in the 0-0.2 mM range for the 224 nm peak whereas the molarities of 0.5 – 1.5 are best using the 277 nm peak. The decrease observed in the molar absorptivity in the 224 nm peak at concentrations from 0.5 to 1.5 mM is due to the saturation of the detector at this molarity, due to the high absorbance. This system must be analyzed for interferences from HNO_3, Eu, and Cm.

The molar absorptivity for 8-hydroxyquinoline was measured in a scoping experiment, but was later found in a paper to be: 2.5 cm/mM at 307.7 nm. This value will be used in the future experiments.

Calculated Distribution values and Separation factors for previous Cloud Point Runs

Values for distribution and separation factors were calculated for previously performed cloud point extraction data. The newly acquired data was grouped with previous data for comparison. Distribution values are calculated from the concentrations of the analyte in each respective phase. The separation factors are the ratio of the distribution of Curium over the distribution of Europium.

As can be seen, there appears to be a difference in the baseline values (the value of the distribution where no extraction is expected). At this time the source of this difference has not been found. Ongoing analysis is underway to correct either the data calculation method, or the data collection method to eliminate the fundamental difference.

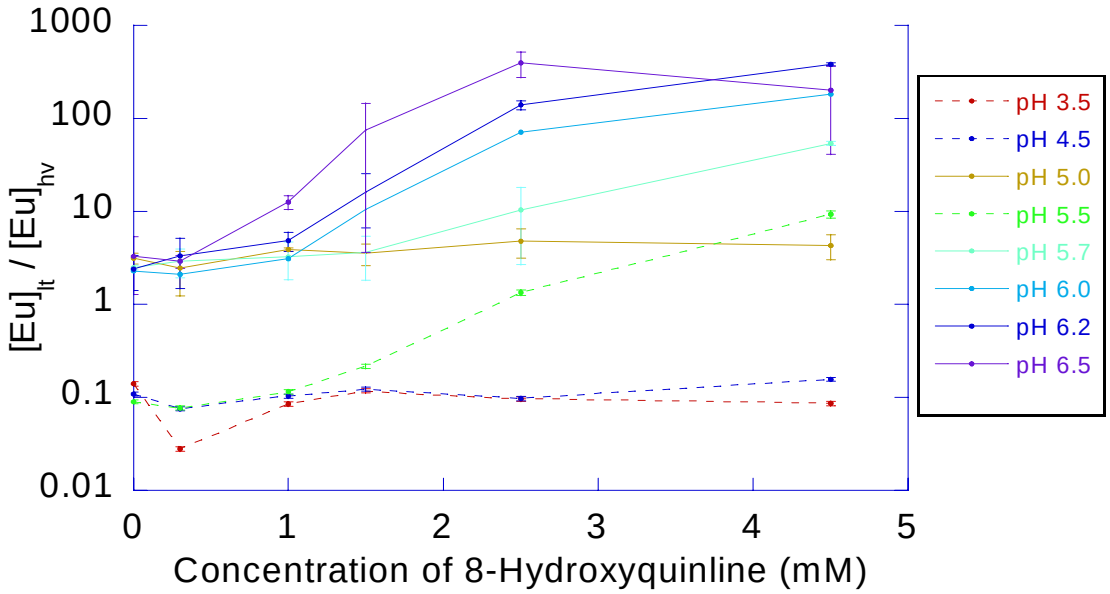

Figure 31. Comparison of distribution data obtained from different individuals in the lab. Dotted lines and solid lines obtained from two individuals.

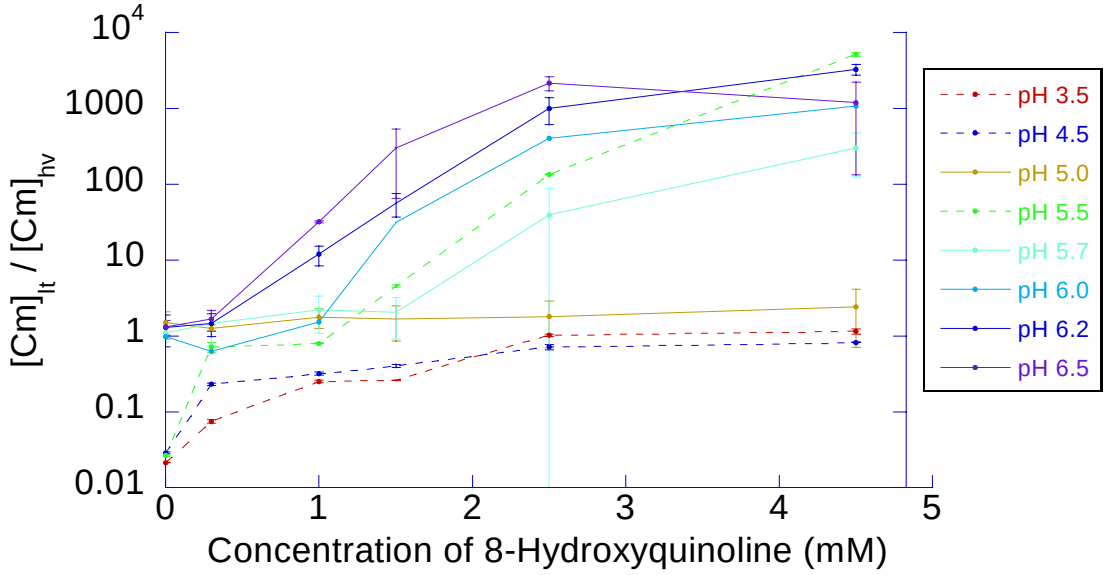

Figure 32. Comparison of Curium distribution data obtained from two individuals in the lab. Dotted and solid lines denote different data sets.

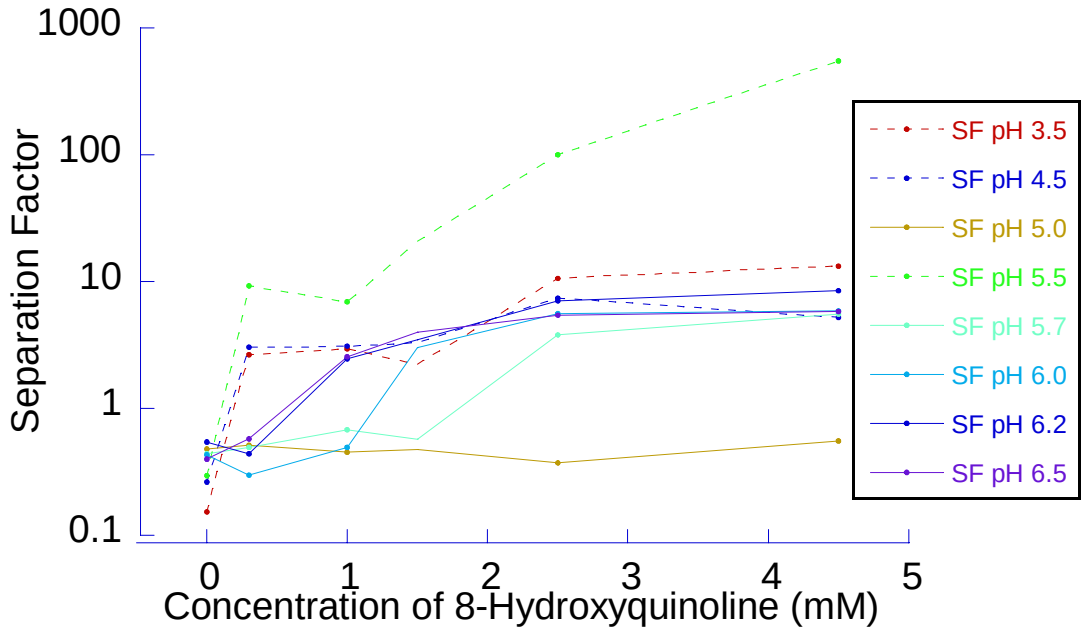

Figure 33. Comparison of two data sets from different individuals in the lab. Dotted and solid lines denote different sets.

Uranium / Beta-SiC Sorption Studies

Uranium sorption studies (UO_2^{2+}) to beta–SiC under atmospheric conditions have been extended from the initial study conditions: 3442 hrs, pH= 2.7±0.2, uranium concentrations of $1.5x10^{-7}$M, $1.16x10^{-6}$M, $5.82x10^{-6}$M to pH values of 3, 5, 5.65, 7 and 9 and are continuing through 1056 hours. The current experiments were started with uranium concentrations matching the initial study, but preliminary data indicates that uranium at the two lowest concentrations is rapidly and completely sorbed to the beta-SiC at pH values above 3. To allow the development of equilibrium states that can be used to determine the maximum K_d values for these systems, uranium concentrations were increased to preclude complete sorption of uranium to the beta-SiC. For the current pH=3 experiments the uranium concentrations are set at $1.16x10^{-6}$M, $5.82x10^{-6}$M and $1.16x10^{-5}$M. For the pH 5-9 experiments the uranium concentrations are set at $5.82x10^{-6}$M, $6.98x10^{-6}$M and $1.16x10^{-5}$M.

Log K_d (ml/g) values for the experiments are given in Table 5 and plotted in Figure 34. The data indicates that there is a break in the behavior of the system between pH 3 and pH 5.65, with pH 5 acting as the transitional zone. At pH 3, as uranium concentrations are increased, the log K_d values decline indicating that the surface of the beta-SiC is fully loaded with uranium at concentrations as low as 1.50e-7 M. The data at pH 5 and pH 5.65 have steady log K_d values with the increasing uranium concentrations being studied in these experiments. This behavior indicates that the surface phase and aqueous phase uranium have established a steady state system, where the beta-SiC surface is not fully loaded, but the surface loading will increase with increasing aqueous uranium concentrations to maintain this state. Both pH 7 and pH 9 indicate increasing log K_d values with increasing uranium concentrations. The trend in the data indicates that a plateau may be reached where the surface of the beta-SiC is loaded to the point where an aqueous phase/surface phase equilibrium is achieved like that of the pH 5 and pH 5.65 data.

[U] M	pH=3	pH=5	pH=5.65	pH=7	pH=9
1.50e-7	2.47			2.44	2.44
1.16e-6	2.26	3.16	3.46	3.16	2.85
5.82e-6	1.91	3.16	3.56	3.68	3.68
6.98e-6		3.16	3.34	3.55	3.77
1.16e-5	0.94	3.12	3.55	3.85	3.85

Table 5. log Kd (ml/g) for uranium and beta-SiC.

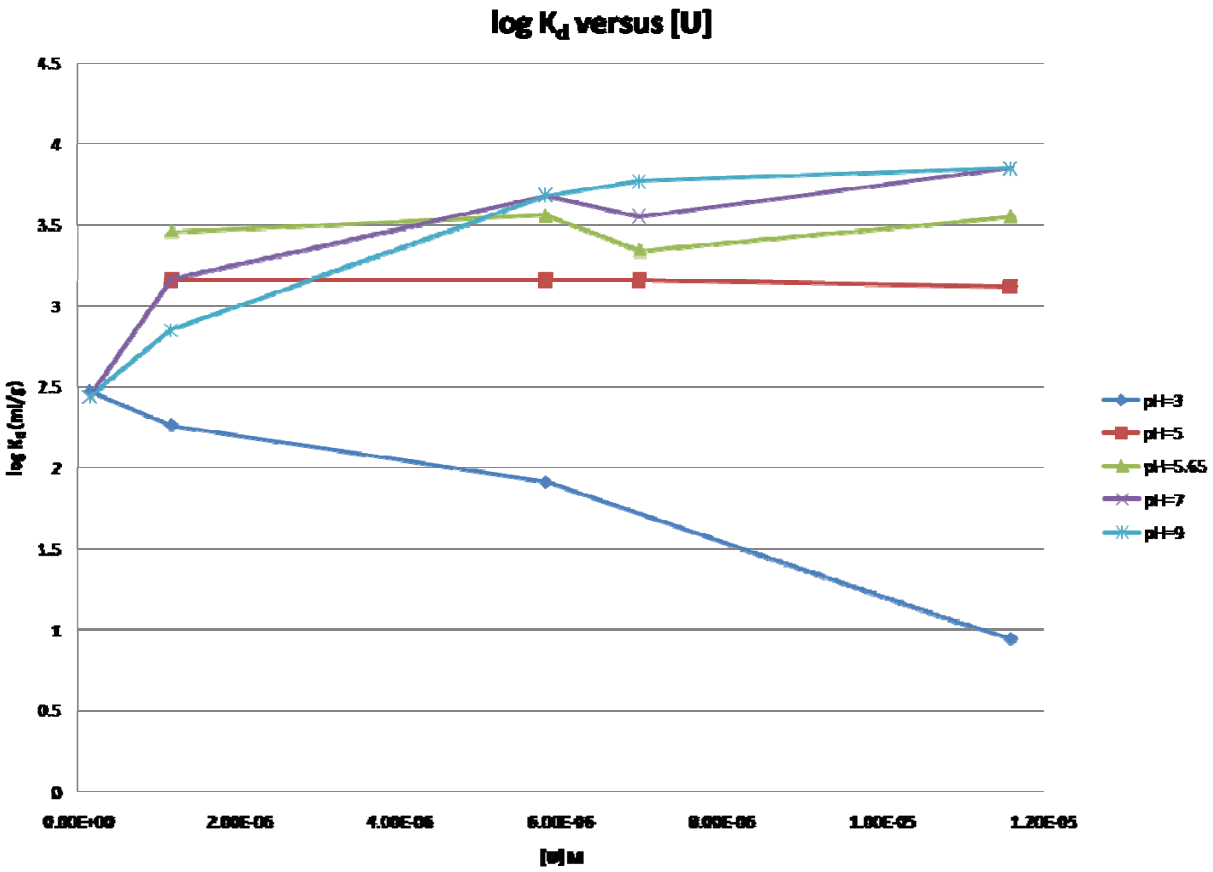

Figure 34. log K_d versus [U] M as a function of pH.

Maximum uranium loading of beta-SiC within this system seems to favor neutral to slightly basic pH values, but higher uranium concentrations need to be studied to verify this concept. The potential to explore higher uranium concentrations at high pH is limited by the precipitation of $UO_3 \bullet 2H_2O$ as the uranium concentrations are increased. Back extrapolation of data indicate that $UO_3 \bullet 2H_2O$ may begin to precipitate at concentrations as low as 10^{-7}M at pH 7 and 10^{-10}M at pH 9. It is possible that the plateau effect being observed at pH 7 and pH 9 is being driven by the precipitation $UO_3 \bullet 2H_2O$. Analysis by XRD of the solid phase after the experiments are completed will be used to verify the presence of $UO_3 \bullet 2H_2O$.

Zero point charge (zpc) data indicate a pH_{zpc} 8.5 for beta-SiC. Below pH 8.5 the beta-SiC is expected to exhibit a positive net surface charge, above pH 8.5 the beta-SiC should exhibit a negative net surface charge. The dominate aqueous uranium species expected at these pH ranges as modeled by JCHESS 3.0 are as follows: UO_2^{2+} (pH 3), $UO_2(OH)_2$ (aq) (pH 5.65,7), $UO_2(CO_3)_3^{4-}$ (pH 9). The uranium species and the surface charge of the beta-SiC are shown below (Table 6).

At pH 3 both the surface of the beta-SiC and uranium are expected to have net positive charges. This would explain the low affinity of uranium for the surface of beta-SiC and the lower relative log K_d values. Moving from pH 3 through pH 5.65 a transition is seen at pH 5. The solution at pH 5 has higher log K_d values then pH 3, but lower than pH 5.65. This trend reflects the change in the uranium species from pure UO_2^{2+} to a mixture of UO_2^{2+} and $UO_2(OH)_2$. At pH 5.65 the neutral $UO_2(OH)_2$ species, with its electron density spread across the oxygen will be more likely to react with the positive surface of the beta-SiC, resulting in higher log K_d values and the easy transition of the $UO_2(OH)_2$ species from the aqueous phase to the surface phase and vice versa, in essence simulating hydrolysis with the oxides on the surface. At pH 7-9 there are multiple transitions occurring, the beta-SiC is shifting from a positive to negative net surface charge, and the uranium is switching from the neutral $UO_2(OH)_2$ species to the negative $UO_2(CO_3)_3^{4-}$ species. A maximum log K_d value is expected in this pH range, as the repulsive charge effects on both the uranium and the beta-SiC are being minimized.

pH	beta-SiC surface charge	Dominate uranium species	Uranium species charge
3	Positive	UO_2^{2+}	Positive
5	Positive	UO_2^{2+} / $UO_2(OH)_2$ (aq)	Positive/Neutral
5.65	Positive	$UO_2(OH)_2$ (aq)	Neutral
7	Positive	$UO_2(OH)_2$ (aq)	Neutral
9	Negative	$UO_2(CO_3)_3^{4-}$	Negative

Table 6. surface charge condition of beta-SiC and uranium species at a given pH.

Equipment Update: Alpha Spectrometer

Eight new chambers were installed and tested, and the migration from the Windows 98 OS to Windows XP was completed. All 12 chambers have been calibrated and are in use. Thirty two polyethylene plates (Figure 35) were machined to replace the stainless steel sample holders provided with the chambers. The polyethylene plates are easier to clean, and utilize a lipped, disposable steel planchet as contamination barrier. The use of the new sample holders result in reduced background count rates, less cross contamination from high activity samples and require less maintenance then the OEM holder.

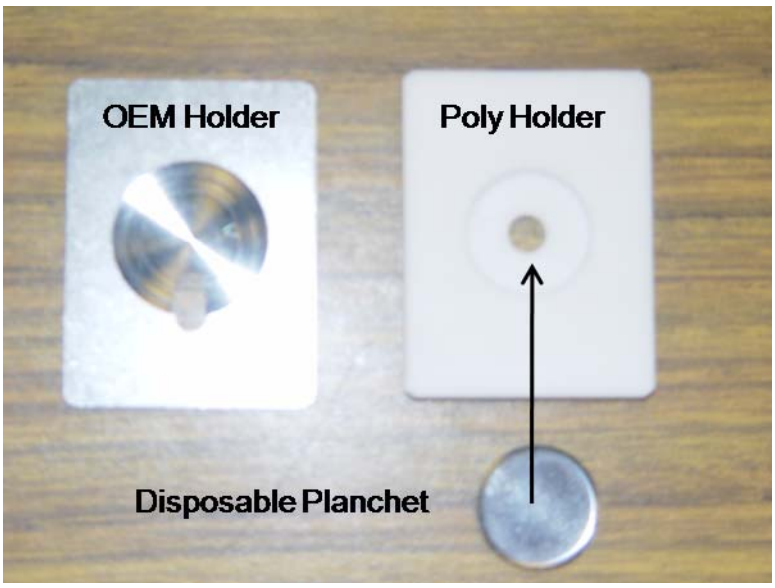

Figure 35. OEM and new alpha spectroscopy sample holders.

Equipment Update: Electroplater

The electroplater has been tested and is now in use. Six polyethylene/PTFE sample holders were constructed (Figure 36) to improve system reliability and safety.

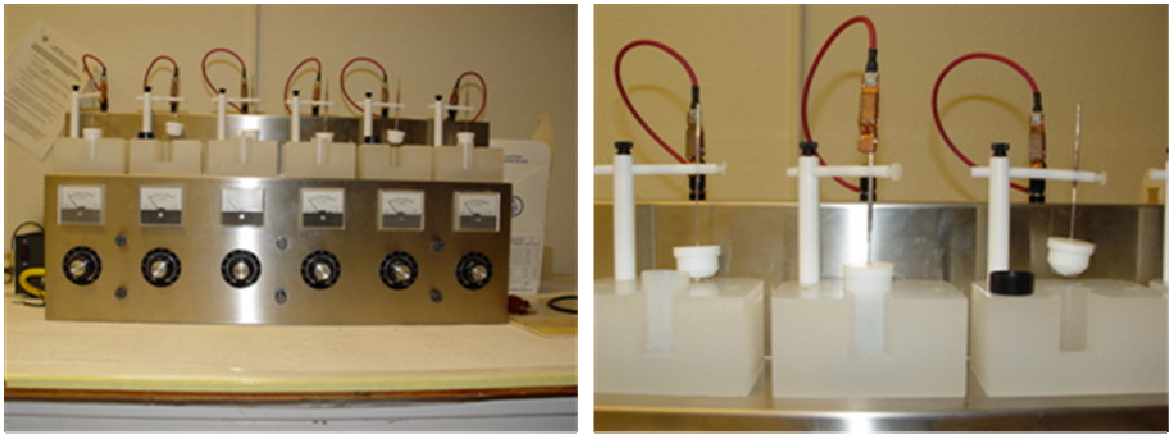

Figure 36. Electoplater and Sample Holder.